A Priori Error Bounds and Parameter Scalings for the Time Relaxation Reduced Order Model

Jorge Reyes[a,*], Ping-Hsuan Tsai[a], Julia Novo[b], Traian Iliescu[a]

[a]*Department of Mathematics, Virginia Tech, Blacksburg, 24060, VA, USA*
[b]*Department of Mathematics, Universidad Autonoma de Madrid, Madrid, 24060, VA, Spain*

Abstract

The *a priori* error analysis of reduced order models (ROMs) for fluids is relatively scarce. In this paper, we take a step in this direction and conduct numerical analysis of the recently introduced time relaxation ROM (TR-ROM), which uses spatial filtering to stabilize ROMs for convection-dominated flows. Specifically, we prove stability, an *a priori* error bound, and parameter scalings for the TR-ROM. Our numerical investigation shows that the theoretical convergence rate and the parameter scalings with respect to ROM dimension and filter radius are recovered numerically. In addition, the parameter scaling can be used to extrapolate the time relaxation parameter to other ROM dimensions and filter radii. Moreover, the parameter scaling with respect to filter radius is also observed in the predictive regime.

Keywords: Reduced order model, Stabilization, Spatial filter, Time relaxation
2020 MSC: 65M12, 65M15, 65M60, 65M70, 76D05, 76F99

1. Introduction

The incompressible Navier-Stokes equations (NSE) are

$$\mathbf{u}_t + (\mathbf{u} \cdot \nabla)\mathbf{u} - \nu\Delta\mathbf{u} + \nabla p = \mathbf{f}, \tag{1}$$

$$\nabla \cdot \mathbf{u} = 0, \tag{2}$$

where $\mathbf{u}$ and p are the velocity and pressure fields, respectively, defined on the spatial domain, Ω, and the time interval, $[0, T]$. $\mathbf{f}$ is an external force, and ν is the inverse of the Reynolds number. Appropriate boundary and initial conditions are needed to close the system.

Fluid flows at high Reynolds numbers exhibit a wide range of spatial and temporal scales that make their direct numerical simulation (DNS) often impractical [1, 2]. This leads to the need of alternative computational approaches, such as large eddy simulations (LES), Reynolds-averaged Navier–Stokes equations (RANS), and numerical regularizations. One type of regularization is the time relaxation model (TRM) [3, 4], which leverages spatial filtering to increase the numerical stability. The TRM for a domain $\Omega \subset \mathbb{R}^d$, $d = 2$ or 3, and for $t > 0$ is given as

$$\mathbf{u}_t + (\mathbf{u} \cdot \nabla)\mathbf{u} - \nu\Delta\mathbf{u} + \chi\mathbf{u}^* + \nabla p = \mathbf{f}, \tag{3}$$

$$\nabla \cdot \mathbf{u} = 0, \tag{4}$$

where the dimensionless parameter χ is called the *time relaxation parameter*, which is often manually tuned to adjust the numerical stabilization, and $\mathbf{u}^*$ is a regularization term defined in Section

---

*Corresponding author

2. The goal of $\mathbf{u}^*$ is to drive the unresolved fluctuations of $\mathbf{u}$ down to 0. TRM has been investigated in [5–11] and has been used in various applications [12, 13]. A TRM review can be found in [14].

Although the DNS computational cost is significantly reduced by LES, RANS, and numerical stabilization, these approaches remain computationally prohibitive in decision-making applications where multiple forward simulations are needed. In those cases, reduced order models (ROMs) represent efficient alternatives. ROMs are computational models whose dimension is orders of magnitude lower than the dimension of full order models (FOMs), i.e., models obtained from classical numerical discretizations. In the numerical simulation of fluid flows, Galerkin ROMs (G-ROMs), which use data-driven basis functions in a Galerkin framework, have provided efficient and accurate approximations of laminar flows, such as the two-dimensional flow past a circular cylinder at low Reynolds numbers [15, 16]. However, turbulent flows are notoriously hard for the standard G-ROM. Indeed, to capture the complex dynamics, a large number [17] of ROM basis functions is required, which yields high-dimensional ROMs that cannot be used in realistic applications. Thus, computationally efficient, low-dimensional ROMs are used instead. Unfortunately, these ROMs are inaccurate since the ROM basis functions that were not used to build the G-ROM have an important role in dissipating the energy from the system [18]. Indeed, without enough dissipation, the low-dimensional G-ROM generally yields spurious numerical oscillations. Thus, closures and stabilization strategies are required for the low-dimensional G-ROMs to be stable and accurate [18–23].

FOM stabilizations and closures are supported by thorough numerical analysis, particularly when applied alongside traditional methods like the finite element method (FEM) or SEM [1, 24–26]. These references address both fundamental numerical analysis issues, such as stability and convergence, and practical challenges, like determining appropriate parameter scalings for stabilization coefficients. These two aspects are closely linked, as insights from numerical analysis guide the selection of parameter scalings, which inform practical decisions. We emphasize, however, that despite growing interest in ROM closures and stabilizations, their comprehensive mathematical and numerical analysis remains an open challenge. Indeed, while some strides have been made in analyzing ROM closures and stabilizations [27–33], much work is needed to reach the rigor of FOM analysis.

In this paper, we take a step in this direction by establishing the first rigorous numerical analysis results, including stability and *a priori* bounds, for the time relaxation reduced order model (TR-ROM), which was successfully used in [34] in numerical simulations of turbulent channel flow. Crucially, we also derive parameter scalings that ensure ROM parameters automatically adjust with changes in the corresponding FOM and ROM parameters, eliminating the need for manual tuning often required in existing data-driven ROMs.

This article is organized as follows: In Section 2, we give preliminaries about the SEM, G-ROM, and ROM filtering. In Section 3, we present the TR-ROM, prove its unconditional stability and an *a priori* error bound, and derive novel scalings for the time relaxation parameter. In Section 4, we show that the theoretical convergence rates and parameter scalings with respect to ROM dimension and filter radius are numerically recovered for the 2D flow past a cylinder and 2D lid-driven cavity. In Section 5, we present the conclusions of our theoretical and numerical investigations.

2. Notations and Preliminaries

2.1. Spectral Element Method

This paper will use the following spaces: $L^p(\Omega)$, $W^{k,p}(\Omega)$, and $H^k(\Omega) = W^{k,2}(\Omega)$, where $k \in \mathbb{N}, 1 \leq p \leq \infty$ for domain Ω. The $L^2(\Omega)$ norm is denoted as $\|\cdot\|$, with the corresponding inner product $(\cdot, \cdot)$. Vector-valued functions are indicated in boldface having d components ($d = 2$ or 3).

The $H^k(\Omega)$ norm will be denoted by $\|\cdot\|_k$, with all other norms clearly denoted. For the continuous vector function $\mathbf{u}(\mathbf{x}, t)$ defined on the entire time interval $(0, T)$, we have

$$\|\mathbf{u}\|_{\infty,k} := \sup_{0<t<T} \|\mathbf{u}(\cdot, t)\|_k, \qquad \text{and} \qquad \|\mathbf{u}\|_{m,k} := \left(\int_0^T \|\mathbf{u}(\cdot, t)\|_k^m \, dt \right)^{\frac{1}{m}}.$$

The solutions are sought in the following functional spaces:

$$\text{Velocity space} - \mathbf{X} := \mathbf{H}_0^1(\Omega) = \left\{ \mathbf{u} \in \mathbf{H}_0^1(\Omega) : \mathbf{u}\mid_{\partial\Omega} = 0 \right\},$$

$$\text{Pressure space} - Q := L_0^2(\Omega) = \left\{ q \in L^2(\Omega) : \int_\Omega q \, d\Omega = 0 \right\},$$

$$\text{Divergence} - \text{free space} - \mathbf{V} := \left\{ \mathbf{v} \in \mathbf{X} : \int_\Omega q \, \nabla \cdot \mathbf{v} \, d\Omega = 0, \ \forall q \in Q \right\}.$$

Boldface indicates that the space is spanned by vector-valued functions. The dual space of $\mathbf{X}$ is denoted as $\mathbf{X}'$, and the norm of the space is $\|\cdot\|_{-1}$. Moreover, we define $\mathbf{V}$ to be the weakly divergence-free subspace of $\mathbf{X}$.

The FOM is based on the SEM in the open-source code Nek5000 [35], and uses the P_{N^-} P_{N-2} velocity-pressure coupling [36]. To this end, let Ω be a polygonal domain and $\{\Omega_i\}_{i=1}^K$ be a conforming partition of Ω into rectangles or rectangular parallelepipeds. If $\mathbf{u}$ is a function defined in $\overline{\Omega} = \cup_{i=1}^K \overline{\Omega}_i$, the restriction of $\mathbf{u}$ to $\overline{\Omega}_i$ will be denoted by $\mathbf{u}_i$. We set

$$\mathbf{X}_N = \left\{ \mathbf{v}_N \in (C^0(\overline{\Omega}))^d \mid (\mathbf{v}_N)_i \in (\mathbb{P}_N(\overline{\Omega}_i))^d, \ (\mathbf{v}_N)_i = 0 \text{ in } \partial\Omega \cap \partial\Omega_i, \ i = 1, \ldots, K \right\},$$

where $\mathbb{P}_N$ denotes the space of polynomials of degree less or equal to N with respect to each variable. The discrete space of pressures $Q_N \subset Q$ is defined as

$$Q_N = \left\{ q_N \in L_0^2(\Omega) \mid (q_N)_i \in \mathbb{P}_{N-2}(\overline{\Omega}_i), \ i = 1, \ldots, K \right\}.$$

The discrete velocity belongs to the space

$$\mathbf{V}_N = \left\{ \mathbf{v}_N \in \mathbf{X}_N \mid (\nabla \cdot \mathbf{v}_N, q_N) = 0 \quad \forall q_N \in Q_N \right\}.$$

With the above choice for the space of pressures, the following inf-sup condition is satisfied [37, 38],

$$\inf_{q_N \in Q_N} \sup_{\mathbf{v}_N \in \mathbf{X}_N} \frac{(q_N, \nabla \cdot \mathbf{v}_N)}{\|q_N\| \|\nabla \mathbf{v}_N\|} \geq \beta N^{\frac{1-d}{2}}, \tag{5}$$

where β is a constant that does not depend on N.

Let Δt denote the time step, and $t^n = n\Delta t$, $n = 0, 1, \ldots, M$, the time instances. We also use the notation $\mathbf{u}(t^n) = \mathbf{u}^n$ and the following discrete norms:

$$\|\|\mathbf{u}\|\|_{\infty,k} := \max_{0 \leq n \leq M} \|\mathbf{u}^n\|_k, \qquad \|\|\mathbf{u}\|\|_{m,k} := \left(\Delta t \sum_{n=0}^M \|\mathbf{u}^n\|_k^m \right)^{1/m}.$$

For $\mathbf{u}, \mathbf{v}, \mathbf{w} \in \mathbf{X}$, we define the trilinear forms $b, b^* : \mathbf{X} \times \mathbf{X} \times \mathbf{X} \mapsto \mathbb{R}$ as follows:

$$b(\mathbf{u}, \mathbf{v}, \mathbf{w}) = (\mathbf{u} \cdot \nabla \mathbf{v}, \mathbf{w}), \tag{6}$$

$$b^*(\mathbf{u}, \mathbf{v}, \mathbf{w}) = (\mathbf{u} \cdot \nabla \mathbf{v}, \mathbf{w}) + \frac{1}{2}((\nabla \cdot \mathbf{u})\mathbf{v}, \mathbf{w}) = \frac{1}{2}(b(\mathbf{u}, \mathbf{v}, \mathbf{w}) - b(\mathbf{u}, \mathbf{w}, \mathbf{v})). \tag{7}$$

3

The following approximation properties hold [37, 38]:

$$\inf_{\mathbf{v}_N \in \mathbf{X}_N} \|\mathbf{u} - \mathbf{v}_N\| \le CN^{-k-1}\|\mathbf{u}\|_{k+1}, \quad \mathbf{u} \in \mathbf{H}^{k+1}(\Omega)^d, \tag{8}$$

$$\inf_{\mathbf{v}_N \in \mathbf{X}_N} \|\nabla(\mathbf{u} - \mathbf{v}_N)\| \le CN^{-k}\|\mathbf{u}\|_{k+1}, \quad \mathbf{u} \in \mathbf{H}^{k+1}(\Omega)^d, \tag{9}$$

$$\inf_{q_N \in Q_N} \|p - q_N\| \le CN^{-s-1}\|p\|_{s+1}, \quad p \in H^{s+1}(\Omega). \tag{10}$$

We also use the following lemmas:

Lemma 2.1. *[39, 40], For* $\mathbf{u}, \mathbf{v}, \mathbf{w} \in \mathbf{X}$, $b^*(\mathbf{u}, \mathbf{v}, \mathbf{w})$ *can be bounded as follows:*

$$b^*(\mathbf{u}, \mathbf{v}, \mathbf{w}) \le C \|\mathbf{u}\|^{\frac{1}{2}} \|\nabla \mathbf{u}\|^{\frac{1}{2}} \|\nabla \mathbf{v}\| \|\nabla \mathbf{w}\|, \tag{11}$$

$$b^*(\mathbf{u}, \mathbf{v}, \mathbf{w}) \le C \|\nabla \mathbf{u}\| \|\nabla \mathbf{v}\| \|\nabla \mathbf{w}\|, \tag{12}$$

$$b^*(\mathbf{u}, \mathbf{v}, \mathbf{w}) \le C \|\nabla \mathbf{u}\| \|\nabla \mathbf{v}\| \|\mathbf{w}\|^{1/2} \|\nabla \mathbf{w}\|^{1/2}. \tag{13}$$

Lemma 2.2 (Discrete Gronwall Lemma [41])**.** *Let* Δt, H, *and* a_n, b_n, c_n, d_n *(for integers* $n \ge 0$*) be finite nonnegative numbers such that*

$$a_l + \Delta t \sum_{n=0}^{l} b_n \le \Delta t \sum_{n=0}^{l} d_n a_n + \Delta t \sum_{n=0}^{l} c_n + H \quad for \quad l \ge 0.$$

Suppose that $\Delta t d_n < 1 \, \forall n$. *Then,*

$$a_l + \Delta t \sum_{n=0}^{l} b_n \le \exp\left(\Delta t \sum_{n=0}^{l} \frac{d_n}{1 - \Delta t d_n}\right)\left(\Delta t \sum_{n=0}^{l} c_n + H\right) \quad for \quad l \ge 0.$$

Let $\mathbf{u}$ be the velocity of the Navier-Stokes equations for a given initial condition, and let $\mathbf{u}_N$ be its continuous in time spectral element approximation. Then, the following bound for the error is proved in [42] (see Remarks 4.2 and 4.3):

$$\|\mathbf{u}(t) - \mathbf{u}_N(t)\| + (N)^{-1}\|\nabla(\mathbf{u}(t) - \mathbf{u}_N(t))\| \le CN^{-(k+1)}, \; t \in (0, T],$$

assuming $\mathbf{u}(t) \in \mathbf{H}^{k+1}(\Omega)$ ($d = 2$).

Using standard techniques, one can also prove error bounds for the fully discrete method. In particular, we will make the following assumption:

Assumption 2.1 (Spectral Element Error)**.** *Under sufficient regularity of the true solution, we assume that the fully discrete approximation of* (1)-(2) *using SEM in space and [BDF3/EXT3] in time,* $\mathbf{u}_N^n \in \mathbf{X}_N$ *for* $1 \le n \le M$, *satisfies the following asymptotic error estimate:*

$$\|\mathbf{u}^n - \mathbf{u}_N^n\|^2 \le C(N^{-2k-2} + \Delta t^6), \qquad \|\nabla(\mathbf{u}^n - \mathbf{u}_N^n)\|^2 \le C(N^{-2k} + \Delta t^6).$$

Remark 2.1. *As discussed in [43],* $k = 3$ *is used to ensure that the imaginary eigenvalues associated with skew-symmetric advection operator are within the stability region of the BDF3/EXT3 time-stepper.*

2.2. Galerkin Reduced Order Model (G-ROM)

In this section, we introduce the G-ROM. We follow the standard proper orthogonal decomposition (POD) procedure [44, 45] to construct the reduced basis function. To this end, we collect a set of spectral element (FOM) solutions lifted by the zeroth mode $\boldsymbol{\varphi}_0$. The POD method seeks a low-dimensional basis $\{\boldsymbol{\varphi}_1, \ldots, \boldsymbol{\varphi}_r\}$ in $\mathbf{L}^2$ that optimally approximates the snapshots, that is, solves the minimization problem:

$$\min \frac{1}{M+1} \sum_{l=0}^{M} \left\| \mathbf{u}_N(\cdot, t_l) - \sum_{j=1}^{r} \left(\mathbf{u}_N(\cdot, t_l), \boldsymbol{\varphi}_j(\cdot) \right) \boldsymbol{\varphi}_j(\cdot) \right\|^2$$

subject to the conditions $(\boldsymbol{\varphi}_i, \boldsymbol{\varphi}_j) = \delta_{ij}$, for $1 \leq i, j \leq r$, where δ_{ij} is the Kronecker delta. The minimization problem can be solved by considering the eigenvalue problem $\mathcal{K}\underline{z}_j = \lambda_j \underline{z}_j$, for $j = 1, \ldots, r$, where $\mathcal{K} \in \mathbb{R}^{(M+1) \times (M+1)}$ is the snapshot Gramian matrix using the L^2 inner product (see, e.g., [21, 46] for alternative strategies).

The first r POD basis functions $\{\boldsymbol{\varphi}_i\}_{i=1}^{r}$ are constructed from the first r eigenmodes of the Gramian matrix. The G-ROM is then constructed by inserting the POD approximated solution $\mathbf{u}_r(\mathbf{x}) = \sum_{j=1}^{r} u_{r,j} \boldsymbol{\varphi}_j(\mathbf{x})$ into the weak form of the NSE: *Find $\mathbf{u}_r$ such that, for all $\mathbf{v}_r \in \mathbf{X}_r$,*

$$\left(\frac{\partial \mathbf{u}_r}{\partial t}, \mathbf{v}_r \right) + Re^{-1} \left(\nabla \mathbf{u}_r, \nabla \mathbf{v}_r \right) + \left((\mathbf{u}_r \cdot \nabla) \mathbf{u}_r, \mathbf{v}_r \right) = 0, \tag{14}$$

where $\mathbf{X}_r := \operatorname{span}\{\boldsymbol{\varphi}_i\}_{i=1}^{r}$ is the ROM space.

It can also be shown that the following error formula holds for the L^2-POD basis functions [47]:

$$\frac{1}{M+1} \sum_{\ell=0}^{M} \left\| \mathbf{u}_N(\cdot, t_\ell) - \sum_{j=1}^{r} \left(\mathbf{u}_N(\cdot, t_\ell), \boldsymbol{\varphi}_j(\cdot) \right) \boldsymbol{\varphi}_j(\cdot) \right\|^2 = \Lambda_{L^2}^r := \sum_{j=r+1}^{R} \lambda_j, \tag{15}$$

where R is the rank of the Gramian matrix, $\mathcal{K}$.

Remark 2.2. *Because the POD basis functions are a linear combination of the snapshots generated from the FOM, the POD basis functions satisfy the boundary conditions of the original PDE and inherit the FOM's divergence-free properties. In this paper, the FOM is based on a SEM discretization, which yields only a weakly divergence-free velocity. More precisely, the POD basis functions belong to $\mathbf{V}_N$, giving $\mathbf{X}_r \subset \mathbf{V}_N$. Thus, to ensure the ROM stability in Lemma 3.1, we equip the ROM with the skew-symmetric trilinear form b^* in (7).*

Additionally, we make use of the following definitions and lemmas:

Definition 2.1 (ROM L^2 Projection). *Let $P_r : \mathbf{L}^2 \to \mathbf{X}_r$ such that, $\forall \, \mathbf{u} \in \mathbf{L}^2, P_r(\mathbf{u})$ is the unique element of $\mathbf{X}_r$ satisfying*

$$(P_r(\mathbf{u}), \mathbf{v}_r) = (\mathbf{u}, \mathbf{v}_r), \ \forall \, \mathbf{v}_r \in \mathbf{X}_r. \tag{16}$$

Lemma 2.3 (H_0^1 POD Projection error). *The POD projection error in the H_0^1 norm satisfies*

$$\frac{1}{M+1} \sum_{\ell=0}^{M} \left\| \mathbf{u}_N(\cdot, t_\ell) - \sum_{j=1}^{r} \left(\mathbf{u}_N(\cdot, t_\ell), \boldsymbol{\varphi}_j(\cdot) \right) \boldsymbol{\varphi}_j(\cdot) \right\|_{\mathbf{H}_0^1}^2 = \Lambda_{H_0^1}^r := \sum_{j=r+1}^{R} \left\| \boldsymbol{\varphi}_j \right\|_{\mathbf{H}_0^1}^2 \lambda_j. \tag{17}$$

Proof. These sharper bounds can be obtained by using the H_0^1 inner product and norm instead of the H^1 inner product and norm in [31, Lemma 3.2]. $\qquad \square$

We list a POD inverse estimate, which will be used in what follows. Let $S_r \in \mathbb{R}^{r \times r}$ with $(S_r)_{ij} = (\nabla \boldsymbol{\varphi}_j, \nabla \boldsymbol{\varphi}_i)$ be the POD stiffness matrix. Let $\|\cdot\|_2$ denote the matrix 2-norm. Since this is traditional notation, in what follows we will use the notation $\|\cdot\|_2$ both for the H^2 norm and for the matrix 2-norm. It will be clear from the context which norm is used.

Lemma 2.4 (POD Inverse Estimates [33])**.** *For all $\mathbf{u}_r \in \mathbf{X}_r$, the following POD inverse estimate holds:*

$$\|\nabla \mathbf{u}_r\| \le \sqrt{\|S_r\|_2} \, \|\mathbf{u}_r\| . \tag{18}$$

The inverse estimate (18) was proved in Lemma 2 and Remark 2 in [48]. The scaling of $\sqrt{\|S_r\|_2}$ with respect to r was numerically investigated in Remark 3.3 in [49] and in Remark 3.2 in [27].

Lemma 2.5 (L^2 Stability of of ROM L^2 Projection [33])**.** *For all $\mathbf{u} \in \mathbf{L}^2$, the ROM projection P_r satisfies*

$$\|P_r(\mathbf{u})\| \le \|\mathbf{u}\| . \tag{19}$$

The following error bound is a slightly modified variation of [31, Lemma 3.3]. This is due to our different spectral element error Assumption 2.1 and different Lemma 2.3. Furthermore, we assume a third-order in time discretization (i.e., BDF3/EXT3) as opposed to the first-order backward Euler method.

Lemma 2.6 (Modified Lemma 3.3 in [31])**.** *For any $\mathbf{u}^n \in \mathbf{X}$, $n = 0, 1, \dots, M$, its L^2 projection, $P_r(\mathbf{u}^n)$, satisfies the following error bounds:*

$$\frac{1}{M+1} \sum_{n=0}^{M} \|\mathbf{u}^n - P_r(\mathbf{u}^n)\|^2 \le C \left(N^{-2k-2} + \Delta t^6 + \Lambda_{L^2}^r \right), \tag{20}$$

$$\frac{1}{M+1} \sum_{n=0}^{M} \|\nabla \left(\mathbf{u}^n - P_r(\mathbf{u}^n) \right)\|^2 \le C \left(N^{-2k} + \|S_r\|_2 \, N^{-2k-2} + (1 + \|S_r\|_2)\Delta t^6 + \Lambda_{H_0^1}^r \right). \tag{21}$$

Proof. The proof of Lemma 2.6 follows a similar approach to that in [31, Lemma 3.3], but here we use the spectral element Assumption 2.1 in place of the finite element error assumption. $\qquad \square$

A generalization of Lemma 2.6 is given by Corollary 2.0.1. This allows a modularity of the projection error to accommodate different discretizations of the FOM.

Corollary 2.0.1. *For any $\mathbf{u}^n \in \mathbf{X}$, $n = 0, 1, \dots, M$, its L^2 projection, $P_r(\mathbf{u}^n) \in X_r$, satisfies the following error bounds:*

$$\frac{1}{M+1} \sum_{n=0}^{M} \|\mathbf{u}^n - P_r(\mathbf{u}^n)\|^2 \le C \left(\|\mathbf{u}^n - \mathbf{u}_{FOM}^n\|^2 + \Lambda_{L^2}^r \right), \tag{22}$$

$$\frac{1}{M+1} \sum_{n=0}^{M} \|\nabla \left(\mathbf{u}^n - P_r(\mathbf{u}^n) \right)\|^2 \le C \left(\|\nabla(\mathbf{u}^n - \mathbf{u}_{FOM}^n)\|^2 + \|S_r\|_2 \|\mathbf{u}^n - \mathbf{u}_{FOM}^n\|^2 + \Lambda_{H_0^1}^r \right). \tag{23}$$

where $\mathbf{u}_{FOM}^n$ is the solution given by the full order model (e.g. FEM, SEM, etc).

We also assume the following bounds, analogous to those in [49]:

Assumption 2.2. *For any $\mathbf{u}^n \in \mathbf{X}$, where $n = 0, 1, \ldots, M$, its L^2 projection, $P_r(\mathbf{u}^n) \in \mathbf{X}_r$, satisfies the following error estimates:*

$$\|\mathbf{u}^n - P_r(\mathbf{u}^n)\|^2 \leq C \left(N^{-2k-2} + \Delta t^6 + \Lambda_{L^2}^r \right), \tag{24}$$

$$\|\nabla (\mathbf{u}^n - P_r(\mathbf{u}^n))\|^2 \leq C \left(N^{-2k} + \|S_r\|_2 \, N^{-2k-2} + (1 + \|S_r\|_2)\Delta t^6 + \Lambda_{H_0^1}^r \right). \tag{25}$$

Remark 2.3 (See also Remark 3.1 in [50].). *The pointwise in time error bounds in Assumption 2.2 are needed in the proof of Theorem 3.1. Specifically, we use those bounds to prove inequalities (49) and (51). We emphasize that using instead the average error bounds in Lemma 2.6 in the proof of Theorem 3.1 would yield suboptimal error bounds (see also [50, Remark 3.1 and Lemma 4.2]).*

Assumption 2.2 and its important effect on the optimality of a priori error bounds was carefully discussed in [51] (see also [31, Remark 3.2]). In particular, it was shown in [51] that using both the snapshots and the snapshot difference quotients to construct the ROM basis yields optimal error bounds without making Assumption 2.2. This result was further improved in [52, 53], where optimal error bounds were proven using only the snapshot difference quotients and the snapshot at the initial time or the mean value of the snapshots. Further improvements were recently presented in [54].

For simplicity, in this paper we do not include the snapshot difference quotients, and instead assume the pointwise in time error bounds in Assumption 2.2.

2.3. ROM filtering

We formally introduce the time relaxation term $\mathbf{u}^* = \mathbf{u} - \bar{\mathbf{u}}$, where $\bar{\mathbf{u}}$ denotes the spatially averaged representation of $\mathbf{u}$. Analogous to what was done for the continuous differential filter G [55, 56] and discrete differential filter G_h [57], we define the ROM differential filter as follows: For $\mathbf{u} \in \mathbf{X}$ and a given filter width $\delta > 0$, we let $G_r : \mathbf{X} \to \mathbf{X}$ be defined by $G_r(\mathbf{u}) := \bar{\mathbf{u}}^r$, where $\bar{\mathbf{u}}^r \in \mathbf{X}$ is the unique solution of the following variational problem:

$$\delta^2 \left(\nabla \bar{\mathbf{u}}^r, \nabla \mathbf{v}_r \right) + (\bar{\mathbf{u}}^r, \mathbf{v}_r) = (\mathbf{u}, \mathbf{v}_r), \ \forall \ \mathbf{v}_r \in \mathbf{X}_r. \tag{26}$$

We note that, when the ROM basis is generated by using the POD strategy, the ROM basis functions (and, thus, the ROM solution) inherit the weakly divergence-free property from the FOM. Leveraging this fact, we do not need to use a Stokes filter, which has been used for weekly preservation of incompressibility [58, 59], and utilize instead G_r as defined in equation (26).

Lemma 2.7. *(ROM Filtering Error Estimate [33]) For $\mathbf{u}^n \in \mathbf{X}$, $n = 0, 1, \ldots, M$, the ROM filter G_r satisfies*

$$\delta^2 \|\nabla (\mathbf{u}^n - G_r(\mathbf{u}^n))\|^2 + \|(\mathbf{u}^n - G_r(\mathbf{u}^n))\|^2 \leq C \left(N^{-2k-2} + \Delta t^6 + \Lambda_{L^2}^r \right) + C\delta^4$$

$$+ C\delta^2 \left(N^{-2k} + \|S_r\|_2 \, N^{-2k-2} + (1 + \|S_r\|_2)\Delta t^6 + \Lambda_{H_0^1}^r \right). \tag{27}$$

Remark 2.4. *The proof of Lemma 2.7 follows along the same lines as the proof of Lemma 4.3 in [33]. The main difference is that one needs to use SEM estimates (Assumption 2.1) instead of FEM estimates. Furthermore, as pointed out in [33, Remark 4.1], since the H^1 stability of the L^2 projection is not available in a ROM setting, the better δ scalings of the H^1 seminorm of the filtering error in [60] cannot be extended to the ROM setting in a straightforward manner.*

It is easy to check that G_r is symmetric and semi-positive definite. The operator is also compact and $\|G_r\| \leq 1$. Its associated eigenvalues satisfy $0 \leq \lambda_j \leq 1$. It is also easy to check that $(I - G_r)$ is symmetric, semi-positive definite, and compact. Moreover, its eigenvalues are $0 \leq 1 - \lambda_j \leq 1$ so

that $\|(I - G_r)\| \leq 1$. Finally, it is easy to check that $G_r\mathbf{u} = \mathbf{u}$ implies $\mathbf{u} = 0$, so that $\lambda_j = 1$ is not an eigenvalue of G_r, and then $(I - G_r)$ is strictly positive definite. This allows us to define the norm:

$$\|\phi\|_* = \sqrt{((I - G_r)\phi, \phi)}. \tag{28}$$

More details on this can be found in [8, Lemma 2.1].

3. Stability and Error Bounds

In this section, we formally introduce our fully discrete TR-ROM. First, in Lemma 3.1, we prove unconditional stability of the new TR-TOM. Then, in Theorem 3.1, we prove an *a priori* error bound for the TR-ROM. Finally, in Section 3.1, we leverage the error bound in Theorem 3.1 to prove parameter scalings for the TR-ROM relaxation parameter, χ.

The fully discrete formulation of the TR-ROM is as follows: For $n = 0, 1, \ldots, M - 2, M - 1$, find $\mathbf{u}_r^{n+1} \in \mathbf{X}_r$ satisfying

$$\frac{1}{\Delta t}(\mathbf{u}_r^{n+1} - \mathbf{u}_r^n, \mathbf{v}_r) + b^*(\mathbf{u}_r^{n+1}, \mathbf{u}_r^{n+1}, \mathbf{v}_r) + \nu(\nabla\mathbf{u}_r^{n+1}, \nabla\mathbf{v}_r)$$
$$+ \chi\left((I - G_r)\mathbf{u}_r^{n+1}, \mathbf{v}_r\right) = (\mathbf{f}(t^{n+1}), \mathbf{v}_r), \quad \forall \mathbf{v}_r \in \mathbf{X}_r. \tag{29}$$

We assume that $\mathbf{u}_r^0$ is the L_2 projection of $\mathbf{u}^0$ into $\mathbf{X}_r$ i.e., $\mathbf{u}_r^0 = P_r(\mathbf{u}^0)$.

To prove the TR-ROM's unconditional stability in Lemma 3.1, we adapt the approach in [5, 10, 61, 62] to the ROM setting.

Lemma 3.1. *The solution to the TR-ROM given by* (29) *is unconditionally stable: For any* $\Delta t > 0$, *the solution satisfies:*

$$\|\mathbf{u}_r^M\|^2 + \nu\||\nabla\mathbf{u}_r^{n+1}\||_{2,0}^2 + 2\chi\Delta t\sum_{n=0}^{M-1}\|\mathbf{u}_r^{n+1}\|_*^2 \leq C_{s,r} := \|\mathbf{u}^0\|^2 + \frac{\Delta t}{\nu}\sum_{n=0}^{M-1}\|\mathbf{f}^{n+1}\|_{-1}^2. \tag{30}$$

Proof. Choosing $\mathbf{v}_r = \mathbf{u}_r^{n+1}$ in (29) yields

$$\left(\frac{\mathbf{u}_r^{n+1} - \mathbf{u}_r^n}{\Delta t}, \mathbf{u}_r^{n+1}\right) + \nu\left(\nabla\mathbf{u}_r^{n+1}, \nabla\mathbf{u}_r^{n+1}\right) + \chi\left((I - G_r)\mathbf{u}_r^{n+1}, \mathbf{u}_r^{n+1}\right) = (\mathbf{f}^{n+1}, \mathbf{u}_r^{n+1})$$

since the skew-symmetric nonlinear term vanishes. After using Cauchy-Schwarz and Young's inequalities, the dual norm of $\mathbf{f}$, and (28), we have

$$\frac{1}{2\Delta t}\left(\|\mathbf{u}_r^{n+1}\|^2 - \|\mathbf{u}_r^n\|^2\right) + \nu\|\nabla\mathbf{u}_r^{n+1}\|^2 + \chi\left\|\mathbf{u}_r^{n+1}\right\|_*^2 \leq \left\|\mathbf{f}(t^{n+1})\right\|_{-1}\left\|\nabla\mathbf{u}_r^{n+1}\right\|$$
$$\leq \frac{\nu}{2}\|\nabla\mathbf{u}_r^{n+1}\|^2 + \frac{\nu^{-1}}{2}\|\mathbf{f}(t^{n+1})\|_{-1}^2.$$

Rearranging some terms and multiplying by $2\Delta t$, we obtain

$$\left(\|\mathbf{u}_r^{n+1}\|^2 - \|\mathbf{u}_r^n\|^2\right) + \nu\Delta t\|\nabla\mathbf{u}_r^{n+1}\|^2 + 2\chi\Delta t\left\|\mathbf{u}_r^{n+1}\right\|_*^2 \leq \frac{\Delta t}{\nu}\|\mathbf{f}(t^{n+1})\|_{-1}^2.$$

Because $\mathbf{u}_r^0$ is the L_2 projection of $\mathbf{u}^0$ onto $\mathbf{X}_r$, summing over time steps yields the following stability bound:

8

$$\|\mathbf{u}_r^M\|^2 + \nu\left(\Delta t \sum_{n=0}^{M-1} \|\nabla\mathbf{u}_r^{n+1}\|^2\right) + 2\chi\left(\Delta t \sum_{n=0}^{M-1} \|\mathbf{u}_r^{n+1}\|_*^2\right)$$

$$\leq \|\mathbf{u}^0\|^2 + \nu^{-1}\left(\Delta t \sum_{n=0}^{M-1} \|\mathbf{f}(t^{n+1})\|_{-1}^2\right). \quad (31)$$

$\square$

To prove the *a priori* error bound in Theorem 3.1, we extend the strategy in [5, 10, 62] to the ROM setting.

Theorem 3.1. *Let $\mathbf{u}_r$ be the solution of the TR-ROM (29), with $\mathbf{u}$ being the true solution of NSE (1)-(2), and let $\mathbf{e}^n = \mathbf{u}^n - \mathbf{u}_r^n$. Under the SE Assumption 2.1, ROM projection Assumption 2.2, and for sufficiently small Δt, we have:*

$$\||\mathbf{e}\||_{\infty,0}^2 + \nu\||\nabla\mathbf{e}^{n+1}\||_{2,0}^2 + 2\chi\Delta t \sum_{n=0}^{M-1} \|\mathbf{e}^{n+1}\|_*^2 \leq CK\Big(\nu^{-1}(N^{-2s-2} + \Delta t^2 + \chi^2\delta^4)$$

$$+ \nu^{-1}\chi^2\left(N^{-2k-2} + \Delta t^6 + \Lambda_{L^2}^r\right) + \nu^{-1}\left(\mathcal{A}(N,\Delta t, S_r, \Lambda_{L^2}^r, \Lambda_{H_0^1}^r) + \sqrt{\Lambda_{L^2}^r}\sqrt{\Lambda_{H_0^1}^r}\right)$$

$$+ \left(\nu + \frac{\chi^2\delta^2 + C_{s,r}}{\nu}\right)\left(N^{-2k} + \|S_r\|_2 N^{-2k-2} + (1 + \|S_r\|_2)\Delta t^6 + \Lambda_{H_0^1}^r\right)\Big), \quad (32)$$

where K depends exponentially on ν^{-3}, C depends on $\mathbf{u}$, $\nabla\mathbf{u}$, $\Delta\mathbf{u}$, $\mathbf{u}_t$, $\mathbf{u}_{tt}$, p, $C(\Omega)$, but not on Δt, N, $\|S_r\|_2$, ν, δ or χ, and $\mathcal{A}$ is defined in (50).

Proof. First, in (33) we introduce a weak formulation of the NSE: Find $(\mathbf{u}, p) \in \mathbf{X} \times Q$ satisfying for all $\mathbf{v}_r \in \mathbf{X}_r$

$$\left(\frac{\mathbf{u}^{n+1} - \mathbf{u}^n}{\Delta t}, \mathbf{v}_r\right) + b^*(\mathbf{u}, \mathbf{u}, \mathbf{v}_r) + \nu(\nabla\mathbf{u}, \nabla\mathbf{v}_r) + \chi((I - G_r)\mathbf{u}^{n+1}, \mathbf{v}_r)$$

$$= \chi((I - G_r)\mathbf{u}^{n+1}, \mathbf{v}_r) + (p, \nabla \cdot \mathbf{v}_r) + \left(\frac{\mathbf{u}^{n+1} - \mathbf{u}^n}{\Delta t} - \mathbf{u}_t, \mathbf{v}_r\right) + (\mathbf{f}, \mathbf{v}_r). \quad (33)$$

We split the error in the usual way as $\mathbf{e}^n = \boldsymbol{\eta}^n + \boldsymbol{\phi}_r^n$, where $\boldsymbol{\eta} = \mathbf{u} - P_r(\mathbf{u})$ and $\boldsymbol{\phi}_r = P_r(\mathbf{u}) - \mathbf{u}_r \in \mathbf{X}_r$, with $P_r(\mathbf{u})$ being the L^2 projection of $\mathbf{u}$ in $\mathbf{X}_r$. Subtract equation (29) from the weak form of the NSE (33) evaluated at t^{n+1} to obtain

$$\frac{1}{\Delta t}(\mathbf{e}^{n+1} - \mathbf{e}^n, \mathbf{v}_r) + b^*(\mathbf{u}^{n+1}, \mathbf{u}^{n+1}, \mathbf{v}_r) - b^*(\mathbf{u}_r^{n+1}, \mathbf{u}_r^{n+1}, \mathbf{v}_r) + \nu(\nabla\mathbf{e}^{n+1}, \nabla\mathbf{v}_r)$$

$$+ \chi((I - G_r)\mathbf{e}^{n+1}, \mathbf{v}_r) = \left(\frac{1}{\Delta t}(\mathbf{u}^{n+1} - \mathbf{u}^n) - \mathbf{u}_t^{n+1}, \mathbf{v}_r\right) + \chi((I - G_r)\mathbf{u}^{n+1}, \mathbf{v}_r)$$

$$+ (p^{n+1}, \nabla \cdot \mathbf{v}_r), \quad \forall\mathbf{v}_r \in \mathbf{X}_r.$$

Note that the nonlinear terms can be rewritten as

$$b^*(\mathbf{u}^{n+1}, \mathbf{u}^{n+1}, \mathbf{v}_r) - b^*(\mathbf{u}_r^{n+1}, \mathbf{u}_r^{n+1}, \mathbf{v}_r) = b^*(\mathbf{e}^{n+1}, \mathbf{u}^{n+1}, \mathbf{v}_r) - b^*(\mathbf{u}_r^{n+1}, \mathbf{e}^{n+1}, \mathbf{v}_r) =$$

$$b^*(\boldsymbol{\eta}^{n+1}, \mathbf{u}^{n+1}, \mathbf{v}_r) - b^*(\boldsymbol{\phi}_r^{n+1}, \mathbf{u}^{n+1}, \mathbf{v}_r) + b^*(\mathbf{u}_r^{n+1}, \boldsymbol{\eta}^{n+1}, \mathbf{v}_r) - b^*(\mathbf{u}_r^{n+1}, \boldsymbol{\phi}_r^{n+1}, \mathbf{v}_r).$$

9

Using the above equality, splitting the error, letting $\mathbf{v}_r = \phi_r^{n+1}$, and noting that $b^*(\mathbf{u}_r^{n+1}, \phi_r^{n+1}, \phi_r^{n+1}) = 0$, we obtain

$$
\begin{aligned}
\frac{1}{2\Delta t} & \left(||\phi_r^{n+1}||^2 - ||\phi_r^n||^2 \right) + \nu||\nabla\phi_r^{n+1}||^2 + \chi \left\| \phi_r^{n+1} \right\|_*^2 = \frac{1}{\Delta t}(\boldsymbol{\eta}^{n+1} - \boldsymbol{\eta}^n, \phi_r^{n+1}) \\
& + \nu(\nabla\boldsymbol{\eta}^{n+1}, \nabla\phi_r^{n+1}) + (\mathbf{u}_t^{n+1} - \frac{1}{\Delta t}(\mathbf{u}^{n+1} - \mathbf{u}^n), \phi_r^{n+1}) + b^*(\boldsymbol{\eta}^{n+1}, \mathbf{u}^{n+1}, \phi_r^{n+1}) \\
& - b^*(\phi_r^{n+1}, \mathbf{u}^{n+1}, \phi_r^{n+1}) + b^*(\mathbf{u}_r^{n+1}, \boldsymbol{\eta}^{n+1}, \phi_r^{n+1}) + (p^{n+1}, \nabla \cdot \phi_r^{n+1}) \\
& + \chi((I - G_r)\boldsymbol{\eta}^{n+1}, \phi_r^{n+1}) + \chi((I - G_r)\mathbf{u}^{n+1}, \phi_r^{n+1}) \\
& \leq |T_1| + |T_2| + |T_3| + |T_4| + |T_5| + |T_6| + |T_7| + |T_8| + |T_9|.
\end{aligned}
\tag{34}
$$

We now bound the above terms. By Definition 2.1, $(\boldsymbol{\eta}, \phi_r) = 0$, which yields

$$
|T_1| = \frac{1}{\Delta t} \left| (\boldsymbol{\eta}^{n+1} - \boldsymbol{\eta}^n, \phi_r^{n+1}) \right| = 0.
\tag{35}
$$

The next five terms are all bounded using standard methods.

$$
|T_2| \leq \frac{\nu}{16}||\nabla\phi_r^{n+1}||^2 + C\nu||\nabla\boldsymbol{\eta}^{n+1}||^2,
\tag{36}
$$

$$
\begin{aligned}
|T_3| & \leq \frac{\nu}{16}||\nabla\phi_r^{n+1}||^2 + C\nu^{-1} \left\| \mathbf{u}_t^{n+1} - \frac{1}{\Delta t}(\mathbf{u}^{n+1} - \mathbf{u}^n) \right\|^2 \\
& \leq \frac{\nu}{16}||\nabla\phi_r^{n+1}||^2 + C\nu^{-1}\Delta t \int_{t^n}^{t^{n+1}} \|\mathbf{u}_{tt}\|^2 \, dt,
\end{aligned}
\tag{37}
$$

$$
\begin{aligned}
|T_4| & = |b^*(\boldsymbol{\eta}^{n+1}, \mathbf{u}^{n+1}, \phi_r^{n+1})| \leq C\sqrt{||\boldsymbol{\eta}^{n+1}||||\nabla\boldsymbol{\eta}^{n+1}||}||\nabla\mathbf{u}^{n+1}||||\nabla\phi_r^{n+1}|| \\
& \leq \frac{\nu}{16}||\nabla\phi_r^{n+1}||^2 + C\nu^{-1}||\boldsymbol{\eta}^{n+1}||||\nabla\boldsymbol{\eta}^{n+1}||||\nabla\mathbf{u}^{n+1}||^2,
\end{aligned}
\tag{38}
$$

$$
\begin{aligned}
|T_5| & = |b^*(\phi_r^{n+1}, \mathbf{u}^{n+1}, \phi_r^{n+1})| \leq C\sqrt{||\phi_r^{n+1}||||\nabla\phi_r^{n+1}||}||\nabla\mathbf{u}^{n+1}||||\nabla\phi_r^{n+1}|| \\
& \leq \frac{\nu}{16}||\nabla\phi_r^{n+1}||^2 + C\nu^{-3}||\nabla\mathbf{u}^{n+1}||^4||\phi_r^{n+1}||^2,
\end{aligned}
\tag{39}
$$

$$
\begin{aligned}
|T_6| & = |b^*(\mathbf{u}_r^{n+1}, \boldsymbol{\eta}^{n+1}, \phi_r^{n+1})| \leq C\sqrt{||\mathbf{u}_r^{n+1}||||\nabla\mathbf{u}_r^{n+1}||}||\nabla\boldsymbol{\eta}^{n+1}||||\nabla\phi_r^{n+1}|| \\
& \leq \frac{\nu}{16}||\nabla\phi_r^{n+1}||^2 + C\nu^{-1}||\mathbf{u}_r^{n+1}||||\nabla\mathbf{u}_r^{n+1}||||\nabla\boldsymbol{\eta}^{n+1}||^2.
\end{aligned}
\tag{40}
$$

For the pressure term, since $\phi_r \in \mathbf{X}_r \subset \mathbf{V}_N$, $(q_N, \nabla \cdot \phi_r^{n+1}) = 0$ can be subtracted and then bounded in the standard way:

$$
|T_7| = \left| (p^{n+1} - q_N, \nabla \cdot \phi_r^{n+1}) \right| \leq \frac{\nu}{16} \left\| \nabla\phi_r^{n+1} \right\|^2 + C\nu^{-1} \inf_{q_N \in Q_N} \left\| p^{n+1} - q_N \right\|^2.
\tag{41}
$$

For T_8, we use the fact that $\|(I - G_r)\eta\| \leq \|\eta\|$, and Cauchy-Schwarz, Poincare-Friedrichs, and Young's inequalities:

$$
|T_8| \leq \chi \left\| \boldsymbol{\eta}^{n+1} \right\| \left\| \phi_r^{n+1} \right\| \leq \frac{\nu}{16} \left\| \nabla\phi_r^{n+1} \right\|^2 + C\chi^2\nu^{-1} \left\| \boldsymbol{\eta}^{n+1} \right\|^2.
\tag{42}
$$

For T_9, we use again Cauchy-Schwarz, Young's, and Poincare-Friedrichs inequalities:

$$
|T_9| \leq \chi \left\| (I - G_r)\mathbf{u}^{n+1} \right\| \left\| \phi_r^{n+1} \right\| \leq \frac{\nu}{16} \left\| \nabla\phi_r^{n+1} \right\|^2 + C\chi^2\nu^{-1} \left\| (I - G_r)\mathbf{u}^{n+1} \right\|^2.
\tag{43}
$$

10

Substituting the bounds (35)-(43) into (34), multiplying by $2\Delta t$, summing up from $n = 0$ to $M-1$, and recalling that $||\phi_r^0|| = 0$ since $\mathbf{u}_r^0 = P_r(\mathbf{u}^0)$, yields:

$$
||\phi_r^M||^2 + \nu\Delta t \sum_{n=0}^{M-1} ||\nabla\phi_r^{n+1}||^2 + 2\chi\Delta t \sum_{n=0}^{M-1} ||\phi_r^{n+1}||_*^2
$$

$$
\leq \quad C\Delta t \sum_{n=0}^{M-1} \nu^{-3}||\nabla\mathbf{u}^{n+1}||^4||\phi_r^{n+1}||^2 + C\nu\Delta t \sum_{n=0}^{M-1} ||\nabla\boldsymbol{\eta}^{n+1}||^2
$$

$$
+ \quad C\nu^{-1}\Delta t \sum_{n=0}^{M-1} ||\boldsymbol{\eta}^{n+1}|| \, ||\nabla\boldsymbol{\eta}^{n+1}|| ||\nabla\mathbf{u}^{n+1}||^2 + C\nu^{-1}\Delta t \sum_{n=0}^{M-1} \inf_{q_N\in Q_N} ||p^{n+1} - q_h||^2
$$

$$
+ \quad C\nu^{-1}\Delta t \sum_{n=0}^{M-1} ||\mathbf{u}_r^{n+1}|| ||\nabla\mathbf{u}_r^{n+1}|| ||\nabla\boldsymbol{\eta}^{n+1}||^2 + C\nu^{-1}\Delta t^2 \int_0^T ||\mathbf{u}_{tt}||^2 dt
$$

$$
+ C\chi^2\nu^{-1}\Delta t \sum_{n=0}^{M-1} ||(I - G_r)\mathbf{u}^{n+1}||^2 + C\chi^2\nu^{-1}\Delta t \sum_{n=0}^{M-1} ||\boldsymbol{\eta}^{n+1}||^2. \tag{44}
$$

Next, we continue to bound the error terms on the right-hand side of (44). Using the approximation properties (10), (20), and (21), we obtain:

$$
C\chi^2\nu^{-1}\Delta t \sum_{n=0}^{M-1} ||\boldsymbol{\eta}^{n+1}||^2 \leq C\chi^2\nu^{-1}\left(N^{-2k-2} + \Delta t^6 + \Lambda_{L^2}^r\right), \tag{45}
$$

$$
C\nu\Delta t \sum_{n=0}^{M-1} ||\nabla\boldsymbol{\eta}^{n+1}||^2 \leq C\nu\left(N^{-2k} + ||S_r||_2 N^{-2k-2} + (1 + ||S_r||_2)\Delta t^6 + \Lambda_{H_0^1}^r\right), \tag{46}
$$

$$
C\nu^{-1}\Delta t \sum_{n=0}^{M-1} \inf_{p_N\in Q_N} ||p^{n+1} - q_N||^2 \leq C\nu^{-1}N^{-2s-2}\Delta t \sum_{n=0}^{M-1} ||p||_{s+1}^2
$$

$$
= C\nu^{-1}N^{-2s-2}|||p|||_{2,s+1}^2 \leq C\nu^{-1}N^{-2s-2}, \tag{47}
$$

$$
C\nu^{-1}\Delta t^2 \int_0^T ||\mathbf{u}_{tt}||^2 dt = C\nu^{-1}\Delta t^2 ||\mathbf{u}_{tt}||_{2,0}^2, \leq C\nu^{-1}\Delta t^2. \tag{48}
$$

For the next bound, we use (21) and Assumption 2.2, resulting in:

$$
C\nu^{-1}\Delta t \sum_{n=0}^{M-1} ||\boldsymbol{\eta}^{n+1}|| ||\nabla\boldsymbol{\eta}^{n+1}|| ||\nabla\mathbf{u}^{n+1}||^2 \leq C\nu^{-1}\Delta t \sum_{n=0}^{M-1} ||\boldsymbol{\eta}^{n+1}|| ||\nabla\boldsymbol{\eta}^{n+1}||
$$

$$
\leq \frac{C}{\nu}\left(N^{-2k-2} + \Delta t^6 + \Lambda_{L^2}^r\right)^{1/2}\left(N^{-2k} + ||S_r||_2 N^{-2k-2} + (1 + ||S_r||_2)\Delta t^6 + \Lambda_{H_0^1}^r\right)^{1/2}
$$

$$
\leq \frac{C}{\nu}\left(N^{-2k-1} + \Delta t^3 N^{-k} + \sqrt{||S_r||_2}N^{-2k-2} + \sqrt{||S_r||_2}N^{-k-1}\Delta t^3\right.
$$

$$
+ \sqrt{1 + ||S_r||_2}N^{-k-1}\Delta t^3 + \sqrt{1 + ||S_r||_2}\Delta t^6 + N^{-k}\sqrt{\Lambda_{L^2}^r} + N^{-k-1}\sqrt{\Lambda_{H_0^1}^r}
$$

$$
\left. + \Delta t^3\sqrt{\Lambda_{H_0^1}^r} + \sqrt{||S_r||_2}N^{-k-1}\sqrt{\Lambda_{L^2}^r} + \sqrt{1 + ||S_r||_2}\Delta t^3\sqrt{\Lambda_{L^2}^r} + \sqrt{\Lambda_{L^2}^r}\sqrt{\Lambda_{H_0^1}^r}\right). \tag{49}
$$

11

For notational convenience, we denote all but the last term in (49) as

$$\mathcal{A}(N, \Delta t, S_r, \Lambda_{L^2}^r, \Lambda_{H_0^1}^r) = N^{-2k-1} + \Delta t^3 N^{-k} + \sqrt{\|S_r\|_2} N^{-k-1} \Delta t^3$$

$$+ \sqrt{1 + \|S_r\|_2} N^{-k-1} \Delta t^3 + \sqrt{1 + \|S_r\|_2} \Delta t^6 + N^{-k} \sqrt{\Lambda_{L^2}^r} + \sqrt{\|S_r\|_2} N^{-2k-2}$$

$$+ (N^{k-1} + \Delta t^3) \sqrt{\Lambda_{H_0^1}^r} + \sqrt{\|S_r\|_2} N^{-k-1} \sqrt{\Lambda_{L^2}^r} + \sqrt{1 + \|S_r\|_2} \Delta t^3 \sqrt{\Lambda_{L^2}^r}. \tag{50}$$

The following term utilizes the stability result from Lemma 3.1 together with the Cauchy-Schwarz inequality and Assumption 2.2

$$C\nu^{-1} \Delta t \sum_{n=0}^{M-1} \|\mathbf{u}_r^{n+1}\| \|\nabla \mathbf{u}_r^{n+1}\| \|\nabla \boldsymbol{\eta}^{n+1}\|^2 \leq C C_{s,r} \nu^{-1} \left(\Delta t \sum_{n=0}^{M-1} \|\nabla \boldsymbol{\eta}^{n+1}\|^4 \right)^{1/2}$$

$$\leq C C_{s,r} \nu^{-1} \left(N^{-2k} + \|S_r\|_2 N^{-2k-2} + (1 + \|S_r\|_2) \Delta t^6 + \Lambda_{H_0^1}^r \right). \tag{51}$$

Using Lemma 2.7, we have the following bound:

$$C\chi^2 \nu^{-1} \Delta t \sum_{n=0}^{M-1} \|(I - G_r)\mathbf{u}^{n+1}\|^2 \leq C\chi^2 \nu^{-1} \left(N^{-2k-2} + \Delta t^6 + \Lambda_{L^2}^r \right) + C\nu^{-1} \chi^2 \delta^4$$

$$+ C\chi^2 \delta^2 \nu^{-1} \left(N^{-2k} + \|S_r\|_2 N^{-2k-2} + (1 + \|S_r\|_2) \Delta t^6 + \Lambda_{H_0^1}^r \right). \tag{52}$$

Thus, using the above bounds, (44) becomes

$$\|\phi_r^M\|^2 + \nu \Delta t \sum_{n=0}^{M-1} \|\nabla \phi_r^{n+1}\|^2 + 2\chi \Delta t \sum_{n=0}^{M-1} \|\phi_r^{n+1}\|_*^2$$

$$\leq C\Delta t \sum_{n=0}^{M-1} \nu^{-3} \|\nabla \mathbf{u}^{n+1}\|^4 \|\phi_r^{n+1}\|^2 + C\nu^{-1}(N^{-2s-2} + \Delta t^2 + \chi^2 \delta^4)$$

$$+ C\nu^{-1} \chi^2 \left(N^{-2k-2} + \Delta t^6 + \Lambda_{L^2}^r \right) + C\nu^{-1} \left(\mathcal{A} + \sqrt{\Lambda_{L^2}^r} \sqrt{\Lambda_{H_0^1}^r} \right)$$

$$+ C \left(\nu + \frac{\chi^2 \delta^2 + C_{s,r}}{\nu} \right) \left(N^{-2k} + \|S_r\|_2 N^{-2k-2} + (1 + \|S_r\|_2) \Delta t^6 + \Lambda_{H_0^1}^r \right). \tag{53}$$

Hence, by the Gronwall inequality from Lemma 2.2 with Δt sufficiently small, i.e., $d_n \Delta t :=$ $C\nu^{-3} \|\nabla \mathbf{u}^n\|^4 \Delta t < 1$, we obtain the following result:

$$\|\phi^M\|^2 + \nu \Delta t \sum_{n=0}^{M-1} \|\nabla \phi_r^{n+1}\|^2 + 2\chi \Delta t \sum_{n=0}^{M-1} \|\phi_r^{n+1}\|_*^2$$

$$\leq C \exp \left(\Delta t \sum_{n=0}^{M-1} \frac{d_n}{(1 - \Delta t \, d_n)} \right) \left(\nu^{-1}(N^{-2s-2} + \Delta t^2 + \chi^2 \delta^4) \right.$$

$$+ \nu^{-1} \chi^2 \left(N^{-2k-2} + \Delta t^6 + \Lambda_{L^2}^r \right) + \nu^{-1} \left(\mathcal{A} + \sqrt{\Lambda_{L^2}^r} \sqrt{\Lambda_{H_0^1}^r} \right)$$

$$+ \left(\nu + \frac{\chi^2 \delta^2 + C_{s,r}}{\nu} \right) \left(N^{-2k} + \|S_r\|_2 N^{-2k-2} + (1 + \|S_r\|_2) \Delta t^6 + \Lambda_{H_0^1}^r \right) \Bigg). \tag{54}$$

The triangle inequality finishes the proof. $\qquad \square$

3.1. Parameter Scalings

In this subsection, we build upon the error bound proved in Theorem 3.1 to derive parameter scalings for the time relaxation constant, χ. To discover the optimal choice of parameter χ, we extend the strategy used in [27] to the ROM setting. To this end, we consider the error bound given by the result of Theorem 3.1:

$$
|||\mathbf{e}|||_{\infty,0}^2 + \nu |||\nabla \mathbf{e}^{n+1}|||_{2,0}^2 + 2\chi \Delta t \sum_{n=0}^{M-1} \|\mathbf{e}^{n+1}\|_*^2 \leq CK \left(\nu^{-1}(N^{-2s-2} + \Delta t^2 + \chi^2 \delta^4) \right.
$$

$$
+ \nu^{-1}\chi^2 \left(N^{-2k-2} + \Delta t^6 + \Lambda_{L^2}^r \right) + \nu^{-1} \left(\mathcal{A} + \sqrt{\Lambda_{L^2}^r} \sqrt{\Lambda_{H_0^1}^r} \right)
$$

$$
+ \left(\nu + \frac{\chi^2 \delta^2 + C_{s,r}}{\nu} \right) \left(N^{-2k} + \|S_r\|_2 N^{-2k-2} + (1 + \|S_r\|_2)\Delta t^6 + \Lambda_{H_0^1}^r \right) \right). \tag{55}
$$

First, we note that following the classical approach (see, e.g., [27]) and attempting to minimize the whole left hand side of (55) would result in only the trivial solution $\chi = 0$. Choosing $\chi = 0$, however, would result in removing the time-relaxation term, which would yield the standard G-ROM. This would clearly be an impractical choice since G-ROM is notoriously inaccurate in the under-resolved regime. Thus, we propose a different strategy and minimize only the time-relaxation term (i.e., the third term) on the LHS of (55). Our choice is further motivated by [63], where it is stated that $\|\mathbf{u}\|_*$ measures the high frequency components of $\mathbf{u}$, which is where spurious oscillations concentrate in the under-resolved regime. To minimize the time-relaxation term, we drop the other two terms on the LHS of (55), and divide by χ. To simplify the notation of the RHS of (55), we define a function F as follows:

$$
F(\chi) := \left(\nu^{-1} \left(\Delta t^2 + N^{-2s-2} + \mathcal{A} + \sqrt{\Lambda_{L^2}^r \Lambda_{H_0^1}^r} \right) + (\nu + \nu^{-1}C_{s,r})\mathcal{H} \right) \chi^{-1}
$$

$$
+ \nu^{-1} \left(\delta^4 + \mathcal{L} + \delta^2 \mathcal{H} \right) \chi, \tag{56}
$$

where

$$
\mathcal{L} := N^{-2k-2} + \Delta t^6 + \Lambda_{L^2}^r, \quad \mathcal{H} := N^{-2k} + \|S_r\|_2 N^{-2k-2} + (1 + \|S_r\|_2)\Delta t^6 + \Lambda_{H_0^1}^r.
$$

Taking the derivative of F with respect to χ in (56) yields

$$
F'(\chi) = - \left(\nu^{-1} \left(\Delta t^2 + N^{-2s-2} + \mathcal{A} + \sqrt{\Lambda_{L^2}^r \Lambda_{H_0^1}^r} \right) + (\nu + \nu^{-1}C_{s,r})\mathcal{H} \right) \chi^{-2}
$$

$$
+ \nu^{-1} \left(\delta^4 + \mathcal{L} + \delta^2 \mathcal{H} \right). \tag{57}
$$

Since $\chi > 0$, setting $F' = 0$ in (57) results in

$$
\nu^{-1} \left(\Lambda_{L^2}^r + \delta^2 \Lambda_{H_0^1}^r + \delta^4 \right) \chi^2 = \left(\nu^{-1} \left(\Delta t^2 + \sqrt{\Lambda_{L^2}^r} \sqrt{\Lambda_{H_0^1}^r} \right) + (\nu + \nu^{-1}C_{s,r})\Lambda_{H_0^1}^r \right). \tag{58}
$$

Solving for χ in (58) gives the optimal parameter scaling for χ:

$$
\chi = \sqrt{\frac{\nu^{-1} \left(\Delta t^2 + N^{-2s-2} + \mathcal{A} + \sqrt{\Lambda_{L^2}^r \Lambda_{H_0^1}^r} \right) + (\nu + \nu^{-1}C_{s,r})\mathcal{H}}{\nu^{-1} \left(\delta^4 + \mathcal{L} + \delta^2 \mathcal{H} \right)}}. \tag{59}
$$

Remark 3.1. *The χ scaling in (59) is dimensionless since the NSE (1) and the numerical analysis results (including the error bound (55)) are dimensionless.*

4. Numerical Results

In this section, we perform a numerical investigation of the theoretical results obtained in Section 3. To this end, we investigate whether the TR-ROM *a priori* error bound in Theorem 3.1 is recovered numerically. In addition, for the theoretical parameter scaling of the time-relaxation constant χ (59) derived in Section 3.1, we investigate if the time-relaxation parameter scalings with respect to the filter radius, δ, and ROM dimension, r, are recovered numerically. The numerical investigation is performed for two test problems: the 2D flow past a circular cylinder at Reynolds number $Re = 100$ (Section 4.2), and the 2D lid-driven cavity at Reynolds number $Re = 15,000$ (Section 4.3).

The numerical investigation in this section focuses on the TR-ROM *a priori* error bound (32) in Theorem 3.1, which depends on the parameters N, Δt, χ, and δ, as well as the ROM truncation errors $\Lambda_{L^2}^r = \sum_{j=r+1}^{R} \lambda_j$ and $\Lambda_{H_0^1}^r = \sum_{j=r+1}^{R} \|\nabla\phi_j\|^2 \lambda_j$ defined in (15) and (17). In our numerical investigation, to measure the TR-ROM accuracy, we use the mean squared errors defined below:

$$\varepsilon_{L^2} = \frac{1}{M+1} \sum_{k=0}^{M} \|P_R \mathbf{u}_N^k - \mathbf{u}_r^k\|^2, \quad \varepsilon_{H_0^1} = \frac{1}{M+1} \sum_{k=0}^{M} \|\nabla(P_R \mathbf{u}_N^k - \mathbf{u}_r^k)\|^2, \tag{60}$$

where $\mathbf{u}_r^k$ is the TR-ROM approximation, and P_R is the ROM L^2 projection (Definition 2.1) onto the R-dimensional reduced space. Specifically, we numerically investigate the rates of the convergence of ε_{L^2} and $\varepsilon_{H_0^1}$ with respect to the ROM truncation errors $\Lambda_{L^2}^r$ and $\Lambda_{H_0^1}^r$, respectively.

Remark 4.1. *The TR-ROM errors in (60) are computed with respect to the projected FOM solution $P_R \mathbf{u}_N^k$ because (i) the considered model problems do not have exact solutions, and (ii) the cost for computing the errors with respect to the projected FOM solution is independent of the number of FOM degrees of freedom, $\mathcal{N}$. Measuring the error with respect to the FOM solution would require a post-processing step. The R value is selected so that the error between $\mathbf{u}_N^k$ and $P_R \mathbf{u}_N^k$ is small.*

4.1. TR-ROM Computational Implementation

The fully discrete formulation TR-ROM (29) is equivalent to the following system:

$$\frac{1}{\Delta t}(\mathbf{u}_r^{n+1} - \mathbf{u}_r^n, \mathbf{v}_r) + b^*(\mathbf{u}_r^{n+1}, \mathbf{u}_r^{n+1}, \mathbf{v}_r) + \nu(\nabla\mathbf{u}_r^{n+1}, \nabla\mathbf{v}_r)$$
$$+ \chi\left(\mathbf{u}_r^{n+1} - \bar{\mathbf{u}}_r^{n+1}, \mathbf{v}_r\right) = (\mathbf{f}(t^{n+1}), \mathbf{v}_r) \tag{61}$$
$$\bar{\mathbf{u}}_r^{n+1} = G_r(\mathbf{u}_r^{n+1}). \tag{62}$$

Equations (61)–(62) are equivalent to the following algebraic system:

$$\frac{1}{\Delta t} M \underline{u}_r^{n+1} + (\underline{u}_r^{n+1})^T B \underline{u}_r^{n+1} + \nu A \underline{u}_r^{n+1} + \chi M(\underline{u}_r^{n+1} - \underline{\bar{u}}_r^{n+1}) = \underline{f}_r^{n+1} \tag{63}$$
$$\underline{\bar{u}}_r^{n+1} = (M + \delta^2 A)^{-1} M \underline{u}_r^{n+1}, \tag{64}$$

where $M_{ij} = (\boldsymbol{\varphi}_i, \boldsymbol{\varphi}_j)$, $A_{ij} = (\boldsymbol{\varphi}_i, \boldsymbol{\varphi}_j)$, and $B_{ijk} = b^*(\boldsymbol{\varphi}_j, \boldsymbol{\varphi}_k, \boldsymbol{\varphi}_i)$ are the reduced mass, stiffness, and advection operators. $\underline{f}_r$ is the forcing vector projected onto the reduced space, and δ is the filter radius. The algebraic system (63)–(64) can be further expressed in a matrix-vector form:

$$\begin{bmatrix} L & -\chi M \\ 0 & I \end{bmatrix} \begin{bmatrix} \underline{u}_r^{n+1} \\ \underline{\bar{u}}_r^{n+1} \end{bmatrix} + \begin{bmatrix} \underline{u}_r^{n+1} \\ \underline{\bar{u}}_r^{n+1} \end{bmatrix}^T \begin{bmatrix} B & 0 \\ 0 & 0 \end{bmatrix} \begin{bmatrix} \underline{u}_r^{n+1} \\ \underline{\bar{u}}_r^{n+1} \end{bmatrix} = \begin{bmatrix} \underline{f}_r^{n+1} \\ (M + \delta^2 A)^{-1} M \underline{u}_r^{n+1} \end{bmatrix}, \tag{65}$$

where L is a linear operator defined as $L = \frac{1}{\Delta t} M + \nu A + \chi M$. The nonlinear system (65) is of size $2r \times 2r$. However, using the relation, $\overline{\underline{u}}_r^{n+1} = (M + \delta^2 A)^{-1} M \underline{u}_r^{n+1}$, the nonlinear system (65) can be simplified to the following $r \times r$ nonlinear system:

$$L\underline{u}_r^{n+1} - \chi M (M + \delta^2 A)^{-1} M \underline{u}_r^{n+1} + (\underline{u}_r^{n+1})^T B \underline{u}_r^{n+1} = \underline{f}_r^{n+1}, \tag{66}$$

where the low-dimensional ($r \times r$) matrix $(M + \delta^2 A)^{-1}$ can be precomputed. We note that here we assumed that the zeroth mode, $\boldsymbol{\varphi}_0$, is a zero velocity field, but the conclusion of simplifying the $2r \times 2r$ nonlinear system to size of $r \times r$ still holds if one has a nontrivial zeroth mode.

We use the open-source code NekROM [64] to construct and solve the TR-ROM defined in (66) for the two test problems described below. We mention that, in the current TR-ROM implementation, the convection term is not in the skew-symmetric form b^*. We note, however, that using the standard trilinear form b does not have a significant impact on the code's numerical stability.

4.2. 2D Flow Past a Cylinder

Our first test problem is the 2D flow past a cylinder at Reynolds number Re $= 100$, which is a canonical test case for ROMs. The computational domain is $\Omega = [-2.5\,D, 17\,D] \times [-5\,D, 5\,D]$, where D is the cylinder diameter, and the cylinder is centered at $[0, 0]$.

The reduced basis functions $\{\boldsymbol{\varphi}_i\}_{i=1}^r$ are constructed by applying the POD procedure to $K = 2001$ snapshots $\{\mathbf{u}^k := \mathbf{u}(\mathbf{x}, t^k) - \boldsymbol{\varphi}_0\}_{k=1}^K$. The snapshots are collected in the time interval $[500, 520]$ (measured in convective time units, D/U, where U is the free-stream velocity), after the von Karman vortex street is developed, with sampling time $\Delta t_s = 0.01$. The zeroth mode, $\boldsymbol{\varphi}_0$, is set to be the FOM velocity field at $t = 500$. TR-ROM is simulated on the same time interval where the snapshots are collected. Thus, we are in the reproduction regime. As the initial condition for the TR-ROM, we choose the zero vector.

4.2.1. Rates of Convergence

We first investigate the rates of convergence of ε_{L^2} and $\varepsilon_{H_0^1}$ with respect to $\Lambda_{L^2}^r$ and $\Lambda_{H_0^1}^r$ in the reproduction regime. To this end, we fix $N = 12$, $s = 0$, $k = 1$, $\Delta t = 2 \times 10^{-3}$, $\delta = 0.04$, $\chi = 0.2$, and vary r. Table 1 shows the magnitude of each term on the right-hand side of the theoretical error estimate (32) with these parameter values. Thus, the theoretical error estimate (32) yields the following rates of convergence:

$$\varepsilon_{L^2} \sim \mathcal{O}(\Lambda_{L^2}^r), \quad \varepsilon_{H_0^1} \sim \mathcal{O}(\Lambda_{H_0^1}^r). \tag{67}$$

Table 1: Magnitude of each term on the right-hand side of the theoretical error estimate (32) with respect to the number of modes, r. Here $N = 12$, $\Delta t = 2 \times 10^{-3}$, $\delta = 0.04$, and $\chi = 0.2$. With these r values, the matrix 2-norm of the POD stiffness matrix $\|S_r\|_2 = \mathcal{O}(1) - \mathcal{O}(10^2)$.

r	N^{-2s-2}	Δt^2	$\chi^2 \delta^4$	$\chi^2 N^{-2k-2}$	$\chi^2 \Lambda_{L^2}^r$	$\sqrt{\Lambda_{L^2}^r \Lambda_{H_0^1}^r}$	N^{-2k}	$\|S_r\|_2 N^{-2k-2}$	$\Lambda_{H_0^1}^r$
2	6.94e-03	4.00e-06	1.02e-07	1.93e-06	2.47e+01	6.04e+03	6.94e-03	1.47e-04	5.91e+04
5	6.94e-03	4.00e-06	1.02e-07	1.93e-06	4.81e+00	2.63e+03	6.94e-03	8.47e-04	5.73e+04
10	6.94e-03	4.00e-06	1.02e-07	1.93e-06	3.05e-02	1.43e+01	6.94e-03	2.30e-03	2.69e+02
20	6.94e-03	4.00e-06	1.02e-07	1.93e-06	4.19e-05	1.35e-02	6.94e-03	9.34e-03	1.73e-01

15

The behavior of the TR-ROM approximation errors ε_{L^2} and $\varepsilon_{H_0^1}$ with respect to $\Lambda_{L^2}^r$ and $\Lambda_{H_0^1}^r$, respectively, is shown in Figs. 1a–1b. In these plots, the ranges of values for $\Lambda_{L^2}^r$ and $\Lambda_{H_0^1}^r$ correspond to the chosen range of values for r, i.e., from $r = 2$ to $r = 8$. The linear regression in the figures yields the following TR-ROM approximation error rates of convergence with respect to $\Lambda_{L^2}^r$ and $\Lambda_{H_0^1}^r$:

$$\varepsilon_{L^2} \sim \mathcal{O}((\Lambda_{L^2}^r)^{0.9316}), \quad \varepsilon_{H_0^1} \sim \mathcal{O}((\Lambda_{H_0^1}^r)^{0.9753}). \tag{68}$$

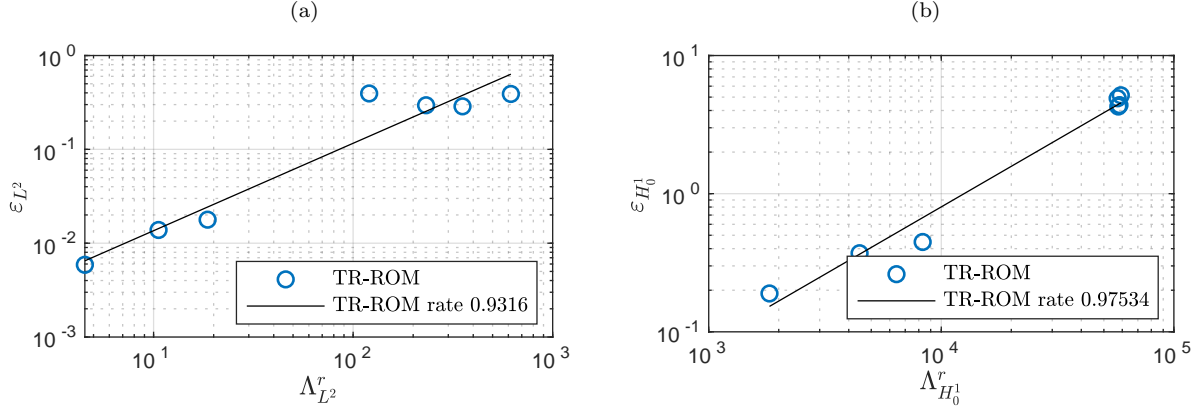Thus, the theoretical rates of convergence (67) are numerically recovered.

Figure 1: 2D flow past a cylinder at Re = 100, TR-ROM with $\chi = 0.2$ and $\delta = 0.04$. (a) Behavior of the mean squared L^2 error ε_{L^2} with respect to $\Lambda_{L^2}^r$, and (b) behavior of the mean squared H_0^1 error $\varepsilon_{H_0^1}$ with respect to $\Lambda_{H_0^1}^r$.

4.2.2. Scaling of χ with respect to δ

In Section 3.1, a theoretical formulation for the time-relaxation constant χ (59) is derived. With $N = 12$, $s = 0$, $k = 1$, and $\Delta t = 2 \times 10^{-3}$, the terms Δt^2, N^{-2s-2}, N^{-2k}, $\|S_r\|_2 N^{-2k-2}$, $(1 + \|S_r\|_2)\Delta t^6$, and $\mathcal{A}$ are relatively small. Hence, (59) can be further simplified as follows:

$$\chi = \sqrt{\frac{\left(\sqrt{\Lambda_{L^2}^r \Lambda_{H_0^1}^r} + C_{s,r}\Lambda_{H_0^1}^r\right)}{\left(\Lambda_{L^2}^r + \delta^2 \Lambda_{H_0^1}^r + \delta^4\right)}}. \tag{69}$$

Given an r value, $C_{s,r}$, $\Lambda_{L^2}^r$, $\sqrt{\Lambda_{L^2}^r \Lambda_{H_0^1}^r}$, and $\Lambda_{H_0^1}^r$ are fixed. Hence, (69) indicates that the theoretical χ, χ_{theory}, scales like either δ^{-1} or δ^{-2}, depending on the δ value. That is, there exist two δ values, δ_1 and δ_2, such that

$$\chi_{\text{theory}} \sim \mathcal{O}(1) \quad \forall \, \delta < \delta_1, \tag{70}$$

$$\chi_{\text{theory}} \sim \mathcal{O}(\delta^{-1}) \quad \forall \, \delta_1 \le \delta < \delta_2, \tag{71}$$

$$\chi_{\text{theory}} \sim \mathcal{O}(\delta^{-2}) \quad \forall \, \delta_2 \le \delta. \tag{72}$$

We investigate whether the scaling of the effective χ, $\chi_{\text{effective}}$, with respect to the filter radius, δ, follows the scaling indicated by (69).

In Fig. 2, the behavior of χ_{theory} in (69) and $\chi_{\text{effective}}$ with respect to the filter radius, δ, is shown for $r = 2$ and 3. $\chi_{\text{effective}}$ is found by solving the TR-ROM and is defined to be the largest χ value that yields an accuracy that is similar to (i.e., within 5% of) the accuracy for the optimal
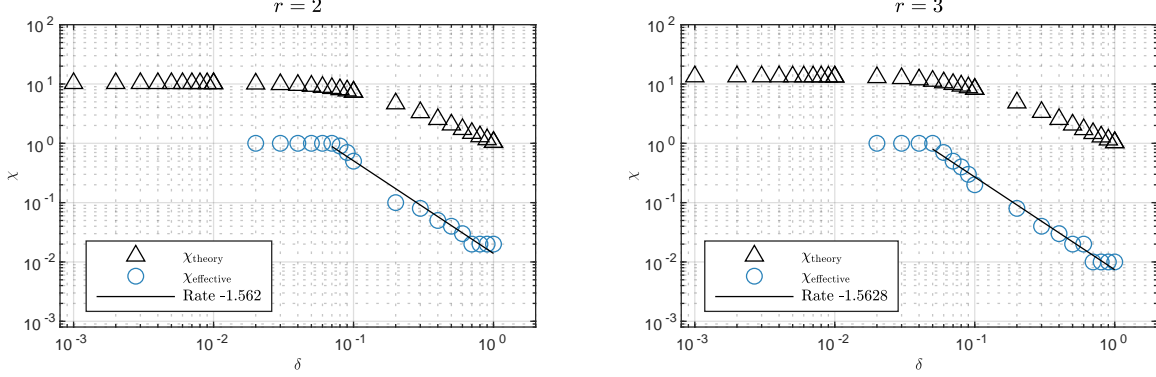
16

Figure 2: 2D flow past a cylinder at Re = 100. Behavior of χ_{theory} (69) and $\chi_{\text{effective}}$ with respect to the filter radius δ for $r = 2$ and 3.

χ, which is defined to be the χ value that yields the smallest $\varepsilon_{H_0^1}$. Specifically, for each r value, we consider 18 δ values from $[0.02, 1]$. For each δ value, 35 χ values from $[0.001, 5]$ are considered, and $\chi_{\text{effective}}$ is selected from the 35 χ values.

The results show that, for both r values, $\chi_{\text{effective}}$ scales like a constant for $\delta \leq \delta_1$, where δ_1 varies with the r value. The linear regression in the figure indicates that $\chi_{\text{effective}}$ scale like $\delta^{-1.56}$ for $\delta > \delta_1$.

Next, we use two δ values to estimate the ratio between the effective χ and the theoretical χ (69), and demonstrate that this ratio can be used with χ_{theory} to *predict* $\chi_{\text{effective}}$ at other δ values. To this end, we compute the ratio between χ_{theory} and $\chi_{\text{effective}}$ at $\delta = 0.2$ and 0.3, and take the average of the two ratios. The extrapolated χ values at $\delta = 0.4, 0.5, 0.6, 0.7$ are then computed using χ_{theory} and the average of the two ratios calculated above. From the results shown in Fig. 3, the extrapolated χ is close to the effective χ, which illustrates the predictive capabilities of the theoretical parameter scaling for χ in (69).
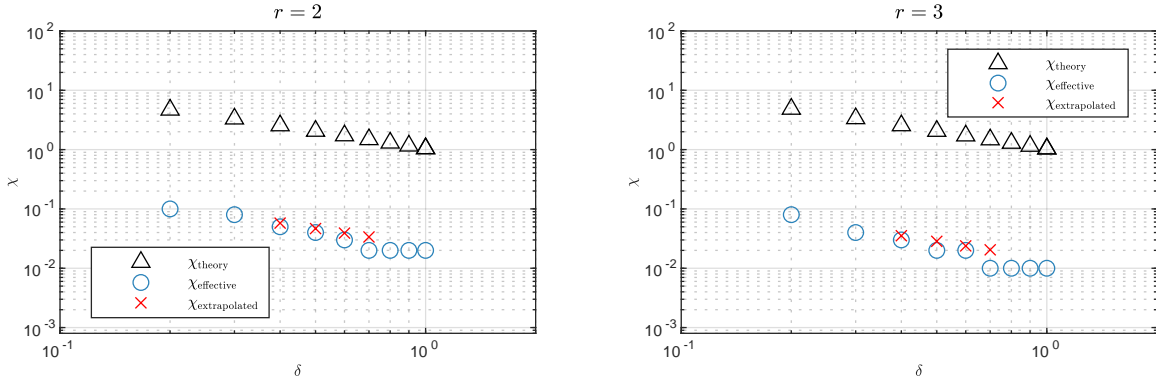

Figure 3: 2D flow past a cylinder at Re = 100. Behavior of the extrapolated χ with respect to the filter radius, δ, for $r = 2$ and 3. Extrapolation is done by using the two values of χ_{theory} (69) and $\chi_{\text{effective}}$ at $\delta = 0.2$ and $\delta = 0.3$.

4.3. 2D Lid-Driven Cavity

Our next example is the 2D lid-driven cavity (LDC) problem at Re = 15,000, which is a more challenging model problem compared to the 2D flow past a cylinder. As demonstrated in [19], the problem requires more than 60 POD modes for G-ROM to accurately reconstruct the solutions and QOIs. A detailed description of the FOM setup for this problem can be found in [21].

The reduced basis functions $\{\varphi_i\}_{i=1}^r$ are constructed by applying POD to $K = 2001$ statistically steady state snapshots $\{\mathbf{u}^k := \mathbf{u}(\mathbf{x}, t^k) - \varphi_0\}_{k=1}^K$. The snapshots are collected in the time interval $[6000, 6040]$ with sampling time $\Delta t_s = 0.02$. The zeroth mode, φ_0, is set to the FOM velocity field at $t = 6000$.

17

4.3.1. Rates of Convergence

We first investigate the rates of convergence of ε_{L^2} and $\varepsilon_{H_0^1}$ with respect to $\Lambda_{L^2}^r$ and $\Lambda_{H_0^1}^r$, respectively. To this end, we fix $N = 8$, $s = 0$, $k = 1$, $\Delta t = 10^{-3}$, $\delta = 0.004$, $\chi = 0.2$, and vary r. Table 2 shows the magnitude of each term on the right-hand side of the theoretical error estimate (32) with these choices of parameters. Thus, the theoretical error estimate (55) yields the rates of

Table 2: Magnitude of each term on the right-hand side of the theoretical error estimate (32) with respect to the number of modes, r. Here $N = 8$, $\Delta t = 10^{-3}$, $\delta = 0.06$, and $\chi = 0.05$. The matrix 2-norm of the POD stiffness matrix $\|S_r\|_2 = \mathcal{O}(10^3) - \mathcal{O}(10^4)$ with the considered r values.

r	N^{-2s-2}	Δt^2	$\chi^2\delta^4$	$\chi^2 N^{-2k-2}$	$\chi^2\Lambda_{L^2}^r$	$\sqrt{\Lambda_{L^2}^r\Lambda_{H_0^1}^r}$	N^{-2k}	$\|S_r\|_2 N^{-2k-2}$	$\Lambda_{H_0^1}^r$
2	1.56e-02	1.00e-06	3.24e-08	6.10e-07	4.30e-03	2.59e+02	1.56e-02	2.86e-01	3.92e+04
4	1.56e-02	1.00e-06	3.24e-08	6.10e-07	2.26e-03	1.35e+02	1.56e-02	3.39e-01	2.01e+04
8	1.56e-02	1.00e-06	3.24e-08	6.10e-07	1.30e-03	7.72e+01	1.56e-02	3.77e-01	1.14e+04
16	1.56e-02	1.00e-06	3.24e-08	6.10e-07	5.63e-04	3.14e+01	1.56e-02	4.42e-01	4.38e+03

convergence in (67).
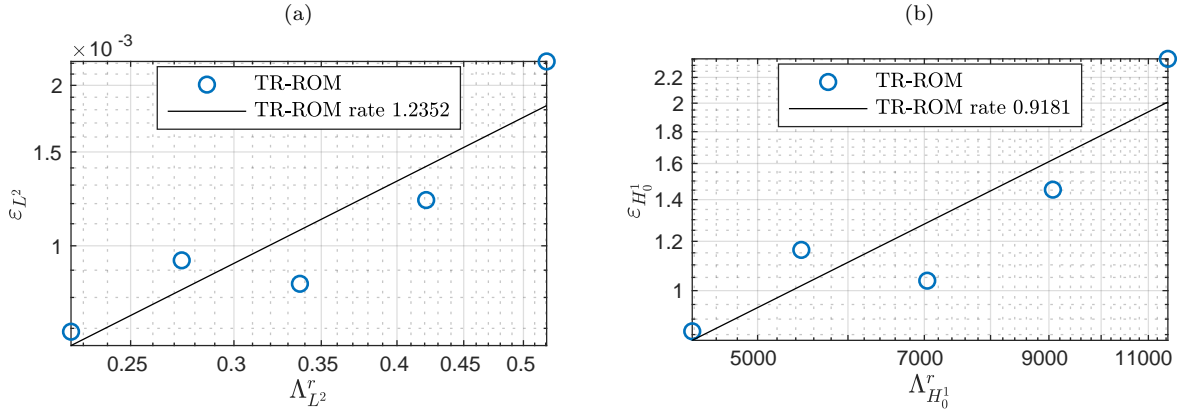

Figure 4: 2D lid-driven cavity at Re $= 15,000$, TR-ROM with $\chi = 0.05$ and $\delta = 0.06$. (a) Behavior of the mean squared L^2 error ε_{L^2} with respect to $\Lambda_{L^2}^r$, and (b) behavior of mean squared H_0^1 error $\varepsilon_{H_0^1}$ with respect to $\Lambda_{H_0^1}^r$. The ranges of $\Lambda_{L^2}^r$ and $\Lambda_{H_0^1}^r$ for the TR-ROM correspond to $r = 8$ to $r = 16$.

The behavior of the TR-ROM approximation errors ε_{L^2} with respect to $\Lambda_{L^2}^r$ and $\varepsilon_{H_0^1}$ with respect to $\Lambda_{H_0^1}^r$, respectively, are shown in Figs. 4a–4b. The ranges of $\Lambda_{L^2}^r$ and $\Lambda_{H_0^1}^r$ correspond to $r = 8$ to $r = 16$. The linear regression in the figures indicates the following TR-ROM approximation error rates of convergence with respect to $\Lambda_{L^2}^r$ and $\Lambda_{H_0^1}^r$:

$$\varepsilon_{L^2} \sim \mathcal{O}((\Lambda_{L^2}^r)^{1.2352}), \quad \varepsilon_{H_0^1} \sim \mathcal{O}((\Lambda_{H_0^1}^r)^{0.9181}). \tag{73}$$

Thus, the theoretical rates of convergence (67) are numerically recovered.

4.3.2. Scaling of χ with respect to δ

With $N = 8$, $s = 0$, $k = 1$ and $\Delta t = 10^{-3}$, the terms Δt^2, N^{-2s-2}, N^{-2k}, $\|S_r\|_2 N^{-2k-2}$, $(1 + \|S_r\|_2)\Delta t^6$, and $\mathcal{A}$ are relatively small. Therefore, (69) holds. Next, we investigate whether the scaling of $\chi_{\text{effective}}$ with respect to the filter radius, δ, follows the scaling in (69) for $r = 4, 8, 12,$ and 16.

In Fig. 5, the behavior of χ_{theory} in (69) and $\chi_{\text{effective}}$ with respect to the filter radius, δ, is shown for $r = 4$ and 16. The results for $r = 8$ and 12 are similar. $\chi_{\text{effective}}$ is found by solving the TR-ROM for different parameter values. Specifically, for each r value, we consider 28 δ values from
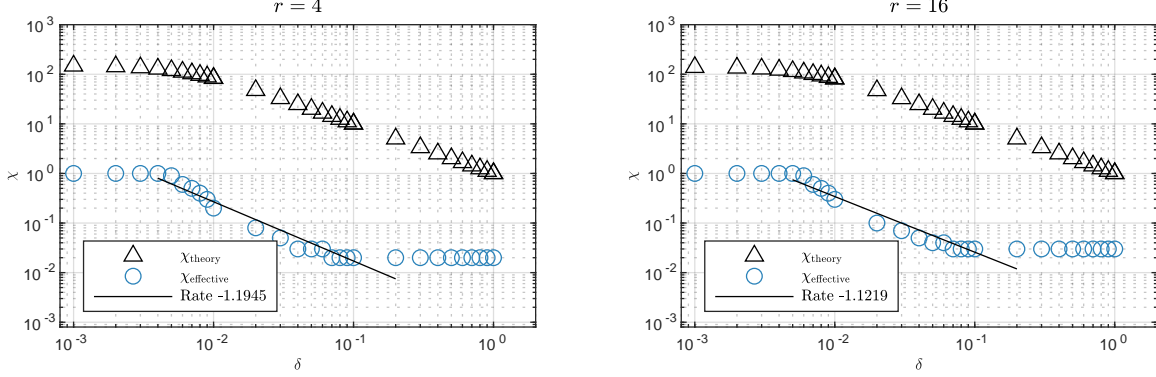
Figure 5: 2D lid-driven cavity at $\text{Re} = 15,000$. Behavior of χ_{theory} (69) and $\chi_{\text{effective}}$ with respect to filter radius, δ, for $r = 4$ and 16.

$[0.001, 1]$. For each δ value, 30 χ values from $[0.001, 1]$ are considered, and $\chi_{\text{effective}}$ is selected from the 30 χ values.

Similar to the 2D flow past a cylinder problem, the results show that $\chi_{\text{effective}}$ scales like a constant for certain $\delta \leq \delta_1$ for all considered r values, where δ_1 varies with the r value. The linear regression in the figure indicates that, for certain $\delta \geq \delta_1$, $\chi_{\text{effective}}$ scales like $\delta^{-1.2}$ for $r = 4$, and scales like $\delta^{-1.1}$ for $r = 16$. Similar scalings are observed in $r = 8$ and $r = 12$ cases. In addition, for $\delta \geq 0.07$, the filtering is too aggressive such that $G_r \mathbf{u}_r \approx \mathbf{0}$. Therefore, the relaxation term $(I - G_r)\mathbf{u}_r$ is dominated by the unfiltered solution, $\mathbf{u}_r$. Hence, we see that $\chi_{\text{effective}}$ does not change for $\delta \geq 0.07$.
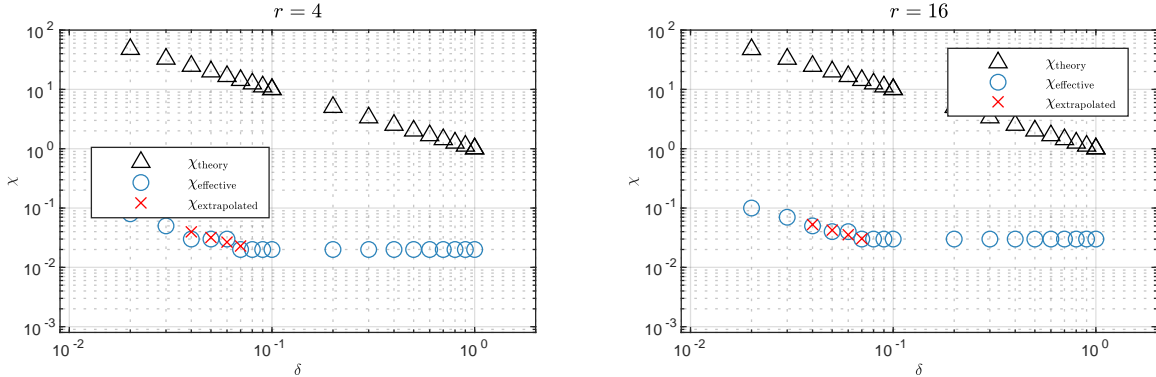

Figure 6: 2D lid-driven cavity at $\text{Re} = 15,000$. Behavior of the extrapolated χ with respect to the filter radius, δ, for $r = 4$ and 16. Extrapolation is done by using the two values of χ_{theory} (69) and $\chi_{\text{effective}}$ at $\delta = 0.02$ and $\delta = 0.03$.

Next, we use two δ values to estimate the ratio between $\chi_{\text{effective}}$ and χ_{theory} (69), and demonstrate that this ratio can be used with χ_{theory} to *predict* $\chi_{\text{effective}}$ at other δ values. To this end, we compute the ratio between χ_{theory} and $\chi_{\text{effective}}$ at $\delta = 0.02$ and 0.03, and take the average of the two ratios. The extrapolated χ values at $\delta = 0.04, 0.05, 0.06,$ and 0.07 are then computed using χ_{theory} and the average of the two ratios calculated above. From the results shown in Fig. 6, the extrapolated χ is close to $\chi_{\text{effective}}$, which highlights the predictive capabilities of the theoretical parameter scalings for χ in (69).

4.3.3. Scaling of χ with respect to r

We also investigate the scaling of $\chi_{\text{effective}}$ with respect to the number of modes, r. First, we note that since $\sqrt{\Lambda_{L^2}^r \Lambda_{H_0^1}^r} \leq \Lambda_{H_0^1}^r$ for $r \in [2, 16]$ (compare columns 7 and 10 in Table 2) and $C_{s,r} = \|\mathbf{u}^0\|^2$,

19

which does not depend on r, the χ in (69) can be further simplified to

$$\chi = \sqrt{\frac{\Lambda^r_{H^1_0}}{\left(\Lambda^r_{L^2} + \delta^2\Lambda^r_{H^1_0} + \delta^4\right)}}. \tag{74}$$

We consider two types of filter radius for studying the scaling of $\chi_{\text{effective}}$ with respect to r. First, we consider a constant filter radius, which is independent of r. In this case, χ_{theory} could scale like $\sqrt{\Lambda^r_{H^1_0}/\Lambda^r_{L^2}}$, a constant related to δ, or $\sqrt{\Lambda^r_{H^1_0}}$, depending on the r value. That is, there exist two r values, r_1 and r_2, such that

$$\chi_{\text{theory}} \sim \mathcal{O}\left(\sqrt{\frac{\Lambda^r_{H^1_0}}{\Lambda^r_{L^2}}}\right) \quad \forall\ r < r_1, \tag{75}$$

$$\chi_{\text{theory}} \sim \mathcal{O}(1) \quad \forall\ r_1 \leq r < r_2, \tag{76}$$

$$\chi_{\text{theory}} \sim \mathcal{O}\left(\sqrt{\Lambda^r_{H^1_0}}\right) \quad \forall\ r_2 \leq r. \tag{77}$$
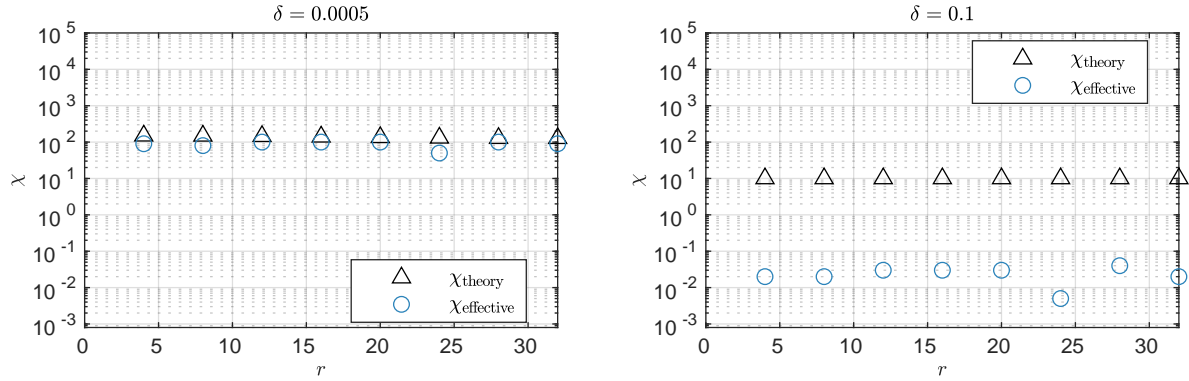

Figure 7: 2D lid-driven cavity at Re $= 15,000$ with constant filter radius. Behavior of χ_{theory} (74) and $\chi_{\text{effective}}$ with respect to number of modes r for $\delta = 0.0005$ and 0.1.

We study the scaling of $\chi_{\text{effective}}$ with respect to r for $\delta = 0.0005$, 0.001, 0.01, and 0.1. In Fig. 7, the behavior of χ_{theory} (74) and $\chi_{\text{effective}}$ with respect to r is shown for $\delta = 0.0005$ and 0.1. For $\delta = 0.0005$, χ_{theory} scales like $\sqrt{\Lambda^r_{H^1_0}/\Lambda^r_{L^2}}$ for the r values considered. Although $\sqrt{\Lambda^r_{H^1_0}/\Lambda^r_{L^2}}$ is a function of r, its dependency on r is weak. Therefore, χ_{theory} behaves like a constant, as shown in the plot. We find that $\chi_{\text{effective}}$ also scales like a constant with respect to r. Specifically, $\chi_{\text{effective}}$ is 100 for almost all r values, except for $r = 8$ and $r = 24$. For $\delta = 0.1$, χ_{theory} scales like a constant for the r values considered. Although $\chi_{\text{effective}}$ is not behaving like a constant, it fluctuates around $\chi = 0.02$. Similar behaviors are observed in $\delta = 0.001$ and $\delta = 0.01$ cases. We also note that $\chi_{\text{effective}}$ at $r = 24$ is much smaller compared to other $\chi_{\text{effective}}$ values for all four δ values. A further investigation is required to gain a better understanding of this behavior.

The second type of filter we consider is the energy-based filter radius δ_{energy} proposed in [22]:

$$\delta_{\text{energy}}(r) = \left(\Lambda h^{2/3} + (1 - \Lambda)L^{2/3}\right)^{3/2}, \text{ where } \Lambda = \sum_{i=1}^{r} \lambda_i / \sum_{i=1}^{R} \lambda_i, \tag{78}$$

L is the characteristic length scale, and h is the mesh size. We emphasize that, in contrast with the constant δ case, $\delta_{\text{energy}}(r)$ is a function of r. Substituting (78) into (74), we find that $\Lambda^r_{H^1_0}\delta^2$ is
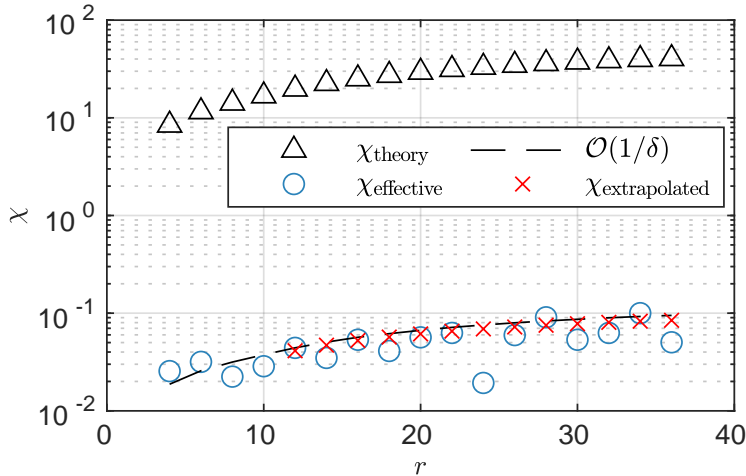
20

Figure 8: 2D lid-driven cavity at Re $= 15,000$ with the energy filter radius δ_{energy} (78). Behavior of χ_{theory} (74), $\chi_{\text{effective}}$, and extrapolated χ with respect to number of modes, r. Extrapolation uses the first four values of χ_{theory} (74) and $\chi_{\text{effective}}$.

the largest term in the denominator for $r = 2$ to $r = 100$. Hence, (74) indicates that χ_{theory} should scale like δ^{-1} for $r \in [0, 100]$. In Fig. 8, the behavior of χ_{theory} in (74) and $\chi_{\text{effective}}$ with respect to r is shown. With the curve defined as $(450\, \delta_{\text{energy}}(r))^{-1}$, we clearly see that $\chi_{\text{effective}}$ also scales like δ^{-1} for the considered r values, just like χ_{theory}.

Next, we use four r values to estimate the ratio between $\chi_{\text{effective}}$ and χ_{theory} (74), and demonstrate that this ratio can be used with χ_{theory} to *predict* $\chi_{\text{effective}}$ at other r values. To this end, we compute the ratio between χ_{theory} and $\chi_{\text{effective}}$ at $r = 4$, 6, 8, and 10, and take the average of the four ratios. The extrapolated χ values at $r = 12$, 14, ..., 36 are then computed using χ_{theory} and the average of the four ratio calculated above. From the results shown in Fig. 8, the extrapolated χ is close to $\chi_{\text{effective}}$ for all r values, except for $r = 24$. This highlights the predictive capabilities of the theoretical parameter scalings for χ in (74).

4.4. Parameter Scaling in the Predictive Regime

In this section, we investigate if, in the *predictive regime*, $\chi_{\text{effective}}$ still scales like δ^{-1}, given by the theoretical parameter scalings for χ in (74). We note that the quantity $\varepsilon_{H_0^1} = \frac{1}{M+1} \sum_{k=0}^{M} \|\nabla(P_R \mathbf{u}_N^k - \mathbf{u}_r^k)\|^2$, which was used to determine $\chi_{\text{effective}}$ in the reproduction regime (Sections 4.2–4.3), is in general sensitive because it is based on the instantaneous error. Hence, in the predictive regime, $\chi_{\text{effective}}$ determined using $\varepsilon_{H_0^1}$ could be sensitive to parameters and deteriorate the parameter scaling. Thus, $\varepsilon_{H_0^1}$ is not a suitable metric for determining $\chi_{\text{effective}}$ in the predictive regime. Therefore, to determine $\chi_{\text{effective}}$ in both the reproduction and predictive regimes, we use an average metric, i.e., the H_0^1 error in the mean field, which is defined as

$$\varepsilon_{H_0^1}^{avg} \equiv \|\langle \mathbf{u}_r \rangle_t - \langle \mathbf{u}_R \rangle_t\|_{H_0^1}^2, \quad \text{where} \quad \langle \mathbf{u}_r \rangle_t := \sum_{k=0}^{M} \mathbf{u}_r^k, \quad \text{and} \quad \langle \mathbf{u}_R \rangle_t := \sum_{k=0}^{M} P_R \mathbf{u}_N^k. \quad (79)$$

The model problem is the 2D lid-driven cavity at Re $= 15,000$, but with a two times larger time interval, that is, $[6000, 6080]$. We consider a larger time interval compared to the previous examples so that the quantity $\langle u_R \rangle_t$ is robust with respect to time.

In Fig. 9, the behavior of $\chi_{\text{effective}}$ in the predictive regime with respect to the filter radius, δ, is shown for $r = 4$ and 16, along with χ_{theory} in (69) and $\chi_{\text{effective}}$ in the reproduction regime. Similar
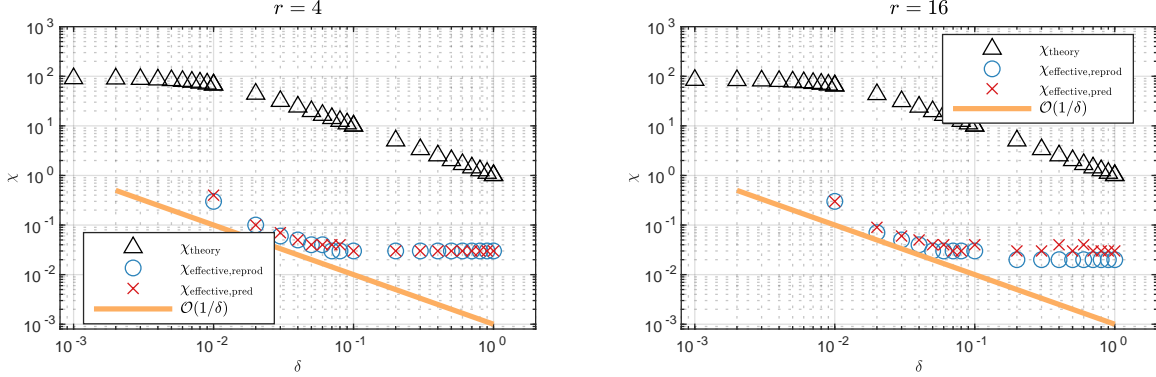
21

Figure 9: Behavior of $\chi_{\text{effective}}$ in predictive regime with respect to filter radius, δ, for $r = 4$ and 16, along with χ_{theory} (69) and $\chi_{\text{effective}}$ in reproduction regime.

results are obtained for $r = 8$ and $r = 12$. To determine $\chi_{\text{effective}}$ in the reproduction regime, for each r value, we simulate TR-ROM in the time interval $[6000, 6080]$ with 19 δ values from $[0.01, 1]$, and 30 χ values from $[0.001, 1]$. For each δ value, $\chi_{\text{effective}}$ in the reproduction regime is selected to be the largest χ value that yields similar accuracy (i.e., within 5%) as that of the optimal χ, which is defined to be the χ value that yields the smallest $\varepsilon_{H_0^1}^{avg}$ in the reproduction regime, with $M = 2001$ samples. To determine $\chi_{\text{effective}}$ in the predictive regime, for each r value, we consider the same parameter ranges for δ and χ as in the reproduction regime and simulate TR-ROM in a time interval $[6000, 6160]$, which is twice as large as the time interval in the reproduction regime. $\chi_{\text{effective}}$ in the predictive regime is selected similarly, but with $M = 4001$ samples, where the last 2000 samples are the data in the predictive regime.

The results show that $\chi_{\text{effective}}$ in the reproduction regime scales like δ^{-1} for the range $0.01 \leq \delta \leq 0.06$. More importantly, the results show that $\chi_{\text{effective}}$ in the predictive regime also scales like δ^{-1} in the same range as in the reproduction regime. In addition, for a given δ value, we observe that $\chi_{\text{effective}}$ in the predictive regime has a similar magnitude as $\chi_{\text{effective}}$ in the reproduction regime.

5. Conclusions

In this work, we performed the first numerical analysis of the recently introduced time-relaxation reduced order model (TR-ROM) [34]. Specifically, we proved unconditional stability in Lemma 3.1 and derived *a priori* error bounds in Theorem 3.1. In addition, in Section 3.1, we leveraged the *a priori* error bounds to derive a formula for the time-relaxation parameter, χ_{theory}, which indicates the scaling of χ with respect to the reduced space dimension r and filter radius δ. A key feature of our analysis is the coupling between the full order model (FOM) and the ROM, as our error bounds include terms related to the FOM discretization, which are critical for developing robust parameter scalings for the time-relaxation parameter, χ. In this study, we employed the spectral element method (SEM) as the FOM, making this the first time that error bounds for SEM-based ROMs have been proven.

In Section 4, we demonstrated that the error convergence rate in Theorem 3.1 and the time-relaxation parameter χ scalings with respect to δ (69) are recovered numerically in two test problems: the 2D flow past a cylinder and 2D lid-driven cavity. In addition, we estimated the ratio between the numerically found χ, denoted as $\chi_{\text{effective}}$, and χ_{theory} at two δ values, and demonstrated that this ratio can be used with χ_{theory} to *predict* $\chi_{\text{effective}}$ at other δ values. Furthermore, for the 2D lid-driven cavity, we demonstrated that the χ scaling with respect to r (74) is recovered numerically for both constant filter radius and energy-based filter radius [22]. Moreover, we showed

that χ_{theory} can be also used to predict $\chi_{\text{effective}}$ at other r values. In Section 4.4, we demonstrated that the $\chi_{\text{effective}}$ scaling with respect δ in the reproduction regime is also observed in the *predictive* regime. In particular, we showed that $\chi_{\text{effective}}$ in the predictive regime has a similar magnitude as $\chi_{\text{effective}}$ in the reproduction regime for most δ values. This illustrates the practical value of the new parameter scaling.

For future work, there are several promising research directions to explore. These include performing numerical analysis (e.g., deriving *a priori* error bounds) for nonlinear filtering and data-driven extensions of the new TR-ROM and other regularized ROMs. These *a priori* error bounds could then be leveraged to determine new ROM parameter scalings. Finally, these scalings could be tested in the predictive regime of challenging numerical simulations (e.g., turbulent channel flow) to determine their range of applicability in practical settings.

6. Acknowledgments

References

[1] L. Berselli, T. Iliescu, W. Layton, Mathematics of Large Eddy Simulation of Turbulent Flows, Scientific Computation, Springer-Verlag, Berlin, 2006.

[2] W. J. Layton, L. G. Rebholz, Approximate Deconvolution Models of Turbulence: Analysis, Phenomenology and Numerical Analysis, Vol. 2042, Springer Berlin Heidelberg, 2012.

[3] S. Stolz, N. A. Adams, L. Kleiser, An approximate deconvolution model for large-eddy simulation with application to incompressible wall-bounded flows, Phys. Fluids 13 (4) (2001) 997–1015.

[4] S. Stolz, N. A. Adams, L. Kleiser, The approximate deconvolution model for large-eddy simulations of compressible flows and its application to shock-turbulent-boundary-layer interaction, Phys. Fluids 13 (10) (2001) 2985–3001.

[5] J. Belding, M. Neda, R. Lan, An efficient discretization for a family of time relaxation models, Comput. Methods Appl. Mech. Engrg. 391 (2022) 114510.

[6] J. Belding, M. Neda, F. Pahlevani, Computational study of the time relaxation model with high order deconvolution operator, Results Appl. Math. 8 (2020) 100–111.

[7] A. A. Dunca, M. Neda, Numerical analysis of a nonlinear time relaxation model of fluids, J. Math. Anal. Appl. 420 (2) (2014) 1095–1115.

[8] V. J. Ervin, W. Layton, M. Neda, Numerical analysis of a higher order time relaxation model of fluids, Int. J. Numer. Anal. Model 4 (3) (2007) 648–670.

[9] W. Layton, M. Neda, Truncation of scales by time relaxation, J. Math. Anal. Appl. 325 (2) (2007) 788–807.

[10] M. Neda, X. Sun, L. Yu, Increasing accuracy and efficiency for regularized Navier-Stokes equations, Acta Appl. Math. 118 (2012) 57–79.

[11] A. Takhirov, M. Neda, J. Waters, Modular nonlinear filter based time relaxation scheme for high Reynolds number flows, Int. J. Numer. Anal. Mod. 15 (2018-04-05) (2018) 699.

[12] M. Neda, J. Waters, Finite element computations of time relaxation algorithm for flow ensembles, Appl. Eng. Lett 1 (2016) 51–56.

[13] A. Takhirov, M. Neda, J. Waters, Time relaxation algorithm for flow ensembles, Num. Meth. P.D.E.s 32 (3) (2016) 757–777.

[14] S. Breckling, M. Neda, T. Hill, A review of time relaxation methods, Fluids 2 (3) (2017) 40.

[15] J. S. Hesthaven, G. Rozza, B. Stamm, Certified Reduced Basis Methods for Parametrized Partial Differential Equations, Springer, 2015.

[16] A. Quarteroni, A. Manzoni, F. Negri, Reduced Basis Methods for Partial Differential Equations: An Introduction, Vol. 92, Springer, 2015.

[17] P. Tsai, P. Fischer, E. Solomonik, Accelerating the Galerkin reduced-order model with the tensor decomposition for turbulent flows, arXiv preprint, `http://arxiv.org/abs/2311.03694` (2023).

[18] S. E. Ahmed, S. Pawar, O. San, A. Rasheed, T. Iliescu, B. R. Noack, On closures for reduced order models − A spectrum of first-principle to machine-learned avenues, Phys. Fluids 33 (9) (2021) 091301.

[19] L. Fick, Y. Maday, A. T. Patera, T. Taddei, A stabilized POD model for turbulent flows over a range of Reynolds numbers: Optimal parameter sampling and constrained projection, J. Comp. Phys. 371 (2018) 214–243.

[20] K. Kaneko, P. Fischer, Augmented reduced order models for turbulence, Front. Phys. (2022) 808.

[21] K. Kaneko, P.-H. Tsai, P. Fischer, Towards model order reduction for fluid-thermal analysis, Nucl. Eng. Des. 370 (2020) 110866.

[22] C. Mou, E. Merzari, O. San, T. Iliescu, An energy-based lengthscale for reduced order models of turbulent flows, Nucl. Eng. Des. 412 (2023) 112454.

[23] E. J. Parish, M. Yano, I. Tezaur, T. Iliescu, Residual-based stabilized reduced-order models of the transient convection-diffusion-reaction equation obtained through discrete and continuous projection, Arch. Comput. Methods Eng.To appear (2024).

[24] V. John, Large Eddy Simulation of Turbulent Incompressible Flows, Vol. 34 of Lecture Notes in Computational Science and Engineering, Springer-Verlag, Berlin, 2004, Analytical and Numerical Results for a Class of LES Models.

[25] T. C. Rebollo, R. Lewandowski, Mathematical and Numerical Foundations of Turbulence Models and Applications, Springer, 2014.

[26] H. G. Roos, M. Stynes, L. Tobiska, Robust Numerical Methods for Singularly Perturbed Differential Equations: Convection-Diffusion-Reaction and Flow Problems., 2nd Edition, Vol. 24 of Springer Series in Computational Mathematics, Springer, 2008.

[27] S. Giere, T. Iliescu, V. John, D. Wells, SUPG reduced order models for convection-dominated convection-diffusion-reaction equations, Comput. Methods Appl. Mech. Engrg. 289 (2015) 454–474.

[28] J. Novo, S. Rubino, Error analysis of proper orthogonal decomposition stabilized methods for incompressible flows, SIAM J. Numer. Anal. 59 (1) (2021) 334–369.

[29] M. Gunzburger, T. Iliescu, M. Schneier, A Leray regularized ensemble-proper orthogonal decomposition method for parameterized convection-dominated flows, IMA J. Numer. Anal. 40 (2) (2020) 886–913.

[30] T. Iliescu, Z. Wang, Variational multiscale proper orthogonal decomposition: Convection-dominated convection-diffusion-reaction equations, Math. Comput. 82 (283) (2013) 1357–1378.

[31] T. Iliescu, Z. Wang, Variational multiscale proper orthogonal decomposition: Navier-Stokes equations, Num. Meth. P.D.E.s 30 (2) (2014) 641–663.

[32] V. John, B. Moreau, J. Novo, Error analysis of a SUPG-stabilized POD-ROM method for convection-diffusion-reaction equations, Comput. Math. Appl. 122 (2022) 48–60.

[33] X. Xie, D. Wells, Z. Wang, T. Iliescu, Numerical analysis of the Leray reduced order model, J. Comput. Appl. Math. 328 (2018) 12–29.

[34] P.-H. Tsai, P. Fischer, T. Iliescu, A time-relaxation reduced order model for the turbulent channel flow, J. Comput. Phys.To appear (2024).

[35] P. Fischer, J. Kruse, J. Mullen, H. Tufo, J. Lottes, S. Kerkemeier, Nek5000–open source spectral element CFD solver, Argonne National Laboratory, Mathematics and Computer Science Division, Argonne, IL, https://nek5000.mcs.anl.gov/index.php/MainPage (2008).

[36] Y. Maday, A. T. Patera, Spectral element methods for the incompressible Navier-Stokes equations, State-of-the-art surveys on computational mechanics (A90-47176 21-64). New York (1989) 71–143.

[37] F. Ben Belgacem, C. Bernardi, N. Chorfi, Y. Maday, Inf-sup conditions for the mortar spectral element discretization of the Stokes problem, Numer. Math. 85 (2) (2000) 257–281.

[38] C. Bernardi, Y. Maday, Uniform inf-sup conditions for the spectral discretization of the Stokes problem, Math. Models Methods Appl. Sci. 9 (3) (1999) 395–414.

[39] W. Layton, Introduction to Finite Element Methods for Incompressible, Viscous Flows, SIAM publications, 2008.

[40] R. Temam, Navier-Stokes Equations: Theory and Numerical Analysis, Vol. 2, American Mathematical Society, 2001.

[41] J. G. Heywood, R. Rannacher, Finite-element approximation of the nonstationary Navier-Stokes problem. Part IV: Error analysis for second-order time discretization, SIAM J. Numer. Anal. 27 (2) (1990) 353–384.

[42] J. de Frutos, J. Novo, A spectral element method for the Navier-Stokes equations with improved accuracy, SIAM J. Numer. Anal. 38 (3) (2000) 799–819.

[43] P. Fischer, M. Schmitt, A. Tomboulides, Recent developments in spectral element simulations of moving-domain problems, in: Recent Progress and Modern Challenges in Applied Mathematics, Modeling and Computational Science, Springer, 2017, pp. 213–244.

[44] G. Berkooz, P. Holmes, J. Lumley, The proper orthogonal decomposition in the analysis of turbulent flows, Ann. Rev. Fluid Mech. 25 (1) (1993) 539–575.

[45] S. Volkwein, Proper Orthogonal Decomposition: Theory and Reduced-Order Modelling, Lecture Notes, University of Konstanz`http://www.math.uni-konstanz.de/numerik/personen/volkwein/teaching/POD-Book.pdf` (2013).

[46] P. Tsai, P. Fischer, Parametric model-order-reduction development for unsteady convection, Front. Phys. 10 (2022) 903169.

[47] P. Holmes, J. L. Lumley, G. Berkooz, Turbulence, Coherent Structures, Dynamical Systems and Symmetry, Cambridge, 1996.

[48] K. Kunisch, S. Volkwein, Galerkin proper orthogonal decomposition methods for parabolic problems, Numer. Math. 90 (1) (2001) 117–148.

[49] T. Iliescu, Z. Wang, Are the snapshot difference quotients needed in the proper orthogonal decomposition?, SIAM J. Sci. Comput. 36 (3) (2014) A1221–A1250.

[50] I. Moore, A. Sanfilippo, F. Balarin, T. Iliescu, A priori error bounds for the approximate deconvolution Leray reduced order model, arXiv preprint, `http://arxiv.org/abs/2410.02673` (2024).

[51] B. Koc, S. Rubino, M. Schneier, J. R. Singler, T. Iliescu, On optimal pointwise in time error bounds and difference quotients for the proper orthogonal decomposition, SIAM J. Numer. Anal. 59 (4) (2021) 2163–2196.

[52] S. L. Eskew, J. R. Singler, A new approach to proper orthogonal decomposition with difference quotients, Adv. Comput. Math. 49 (2) (2023) 33.

[53] B. García-Archilla, V. John, J. Novo, Second order error bounds for POD-ROM methods based on first order divided differences, Appl. Math. Lett. 146 (2023) 108836.

[54] B. García-Archilla, J. Novo, Pointwise error bounds in POD methods without difference quotients, arXiv preprint, `http://arxiv.org/abs/2407.17159` (2024).

[55] M. Germano, Differential filters of elliptic type, Phys. Fluids 29 (6) (1986) 1757–1758.

[56] P. Grisvard, Elliptic Problems in Nonsmooth Domains, SIAM, 2011.

[57] S. Kaya, C. C. Manica, Convergence analysis of the finite element method for a fundamental model in turbulence, Math. Models Methods Appl. Sci. 22 (11) (2012) 1250033.

[58] J. Connors, Convergence analysis and computational testing of the finite element discretization of the Navier–Stokes alpha model, Num. Meth. P.D.E.s 26 (6) (2010) 1328–1350.

[59] C. C. Manica, M. Neda, M. Olshanskii, L. G. Rebholz, Enabling numerical accuracy of Navier-Stokes-α through deconvolution and enhanced stability, ESAIM Math. Model. Numer. Anal. 45 (2) (2011) 277–307.

[60] A. A. Dunca, M. Neda, L. G. Rebholz, A mathematical and numerical study of a filtering-based multiscale fluid model with nonlinear eddy viscosity, Comput. Math. Appl. 66 (6) (2013) 917–933.

[61] S. C. Huang, A. Johnson, M. Neda, J. Reyes, H. Tehrani, A generalization of the Smagorinsky model, Appl. Math. Comput. 469 (2024) 128545.

[62] S. Ingimarson, M. Neda, L. Rebholz, J. Reyes, A. Vu, Improved long time accuracy for projection methods for Navier-Stokes equations using EMAC formulation, Int. J. Numer. Anal. Mod. 20 (2) (2023) 176–198.

[63] V. J. Ervin, W. J. Layton, M. Neda, Numerical analysis of filter-based stabilization for evolution equations, SIAM J. Numer. Anal. 50 (5) (2012) 2307–2335.

[64] K. Kaneko, P. Tsai, P. Fischer, NekROM, `https://github.com/Nek5000/NekROM`.